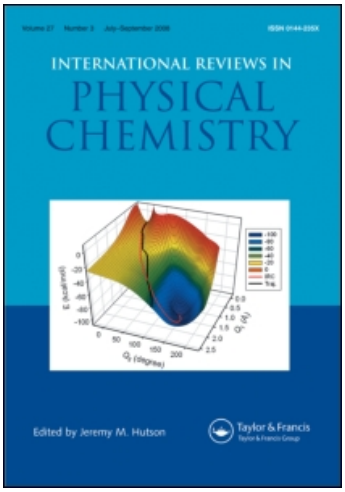

International Reviews in Physical Chemistry
Publication details, including instructions for authors and subscription information:
http://www.informaworld.com/smpp/title~content=t713724383

Radical-radical reaction dynamics: A combined crossed-beam and theoretical study

Jong-Ho Choi[a]
[a] Department of Chemistry and Center for Electro- and Photo-Responsive Molecules, Korea University, Seoul 136-701, Korea

Online publication date: 11 October 2010

To cite this Article Choi, Jong-Ho(2006) 'Radical-radical reaction dynamics: A combined crossed-beam and theoretical study', International Reviews in Physical Chemistry, 25: 4, 613 — 653
To link to this Article: DOI: 10.1080/01442350600867173
URL: http://dx.doi.org/10.1080/01442350600867173

International Reviews in Physical Chemistry,
Vol. 25, No. 4, October–December 2006, 613–653

Taylor & Francis
Taylor & Francis Group

Radical–radical reaction dynamics: A combined crossed-beam and theoretical study

JONG-HO CHOI*

Department of Chemistry and Center for Electro- and Photo-Responsive Molecules, Korea University, 1, Anam-dong, Seoul 136-701, Korea

(*Received 31 March 2006; in final form 4 August 2006*)

We present an overview of our recent studies of the gas-phase reaction dynamics of $O(^3P)$ with a series of hydrocarbon radicals [allyl (C_3H_5), propargyl (C_3H_3), t-butyl (t-C_4H_9)] as prototypal radical–radical oxidation reactions. High-resolution laser spectroscopy in a crossed-beam configuration was applied to examine the nascent rovibrational state distributions and Doppler profiles of the reactive scattering products. The analyses of the product energy and population distributions demonstrated the existence of unusual dynamic characteristics and competition between the addition and abstraction reaction mechanisms at the molecular level. These features, which are in sharp contrast with those of the oxidation reactions of closed-shell hydrocarbon molecules, are discussed with the aid of *ab initio* and quantum statistical calculations.

Contents

*Email: jhc@korea.ac.kr

International Reviews in Physical Chemistry
ISSN 0144–235X print/ISSN 1366–591X online © 2006 Taylor & Francis
http://www.tandf.co.uk/journals
DOI: 10.1080/01442350600867173

1. Introduction

Investigations of gas-phase reaction dynamics provide an intimate understanding of the microscopic mechanisms of elementary chemical processes. Detailed mechanistic studies of the reactions of atomic species such as hydrogen and second-row atoms with small closed-shell molecules have been performed for several decades [1–4]. Notwithstanding their significance, however, little progress has been made in furthering our understanding of radical–radical reactions at the molecular level, particularly in the field of reaction dynamics. Most of the gas-phase investigations conducted so far were restricted to the study of bulk kinetics under thermally relaxed conditions. The lack of information available on this subject is primarily due to the difficulties involved in satisfying the critical prerequisites, such as generating sufficient amounts of clean hydrocarbon radicals, and implementing reliable, facile characterization schemes [5–8]. In the case of the conventional pyrolytic effusion source, the reactive radical species that are generated spend a long residence time inside a hot tube after pyrolysis, which inevitably results in their recombination and/or secondary dissociation. As a result, a mixture of radicals and molecules is generally observed. Such drawbacks have, however, been overcome by adopting the supersonic flash pyrolysis source in short-pulse experiments. Labile precursor molecules inside a high-temperature tube undergo rapid pyrolysis, producing clean, jet-cooled radical beams. Laser spectroscopic methods have been applied to study the photodissociation kinetics and dynamics of several hydrocarbon radicals [9–14].

In bimolecular reactive scattering experiments, only a few studies have been reported so far. Donalson and coworkers studied the exoergic reactions of $O(^3P)$ with vinyl radicals (C_2H_3) using arrested relaxation FT-IR spectroscopy and observed the production of CO with strongly non-statistical vibrational distributions [15, 16].

Bersohn *et al*. investigated the reactions of $O(^3P)$ with methyl radicals (CH_3) under low-pressure flow conditions using the VUV spectroscopic method in order to detect the production of CO, and favoured an indirect addition mechanism to explain the rovibrationally excited states of the products [17]. Recently, Choi and coworkers performed reaction dynamics studies in a crossed-beam configuration to elucidate the mechanistic and dynamic characteristics of the reactions of $O(^3P)$ with organic hydrocarbon radicals [18–26]. On the other hand, theoretical studies of radical–radical reaction dynamics are quite rare, although quite a few calculations have been reported on the oxidation reactions of substituted methyl and unsaturated hydrocarbon radicals [27–30].

This review aims to provide an overview of our recent studies of the gas-phase reaction dynamics of $O(^3P)$ with a series of hydrocarbon radicals, RH [allyl (C_3H_5), propargyl (C_3H_3), t-butyl (t-C_4H_9)], as prototypal radical–radical oxidation reactions. While C_3H_3 and C_3H_5 are simple, unsaturated π-conjugated systems stabilized by resonance structures, t-C_4H_9 is stable as a result of the hyperconjugation resulting from the partial overlap of the sp^3-s orbitals (C–H bonds) with the empty p orbital of the central carbon. These hydrocarbon radicals are well-known reactive species which play a significant role in hydrocarbon synthesis, combustion, interstellar space and atmospheric chemistry, and have long attracted many theoretical and experimental investigations [5, 9, 10, 12, 31–39]. Therefore, the crossed-beam studies of reactive scattering processes can provide important mechanistic details of and insights into radical–radical reaction dynamics as model systems at the microscopic level.

The reaction channel first examined in our crossed-beam experiments was the following exothermic pathway producing a diatomic OH product:

$$O(^3P) + RH \rightarrow OH + R \quad (C_3H_5,\ C_3H_3,\ t\text{-}C_4H_9)$$

A second exothermic reaction was the atomic hydrogen release channel. This pathway was the only channel detected in the previous gas-phase bulk kinetic experiments for the oxidation reactions of allyl and propargyl radicals [40, 41]:

$$O(^3P) + RH \rightarrow H + OR \quad (C_3H_5,\ C_3H_3)$$

High-resolution laser-induced fluorescence (LIF) spectroscopy was used to probe the nascent rovibrational state distributions and Doppler profiles of the reactive scattering products in a crossed-beam configuration. *Ab initio* calculations were carried out, focusing particular attention on the respective reaction pathways, the major reaction channels, and their microscopic kinetics, with the aid of statistical Rice–Ramsperger–Kassel–Marcus (RRKM), prior and surprisal analyses. The unusual mechanistic and dynamic characteristics at the molecular level are discussed.

2. Experiment

Schematic diagrams of the flash pyrolysis source and crossed molecular beam apparatus employed in the experiment are shown in figure 1. The apparatus is designed for the investigation of gas-phase reactive scattering processes, and consists of two source chambers and a scattering chamber [21]. The source chambers are connected to a

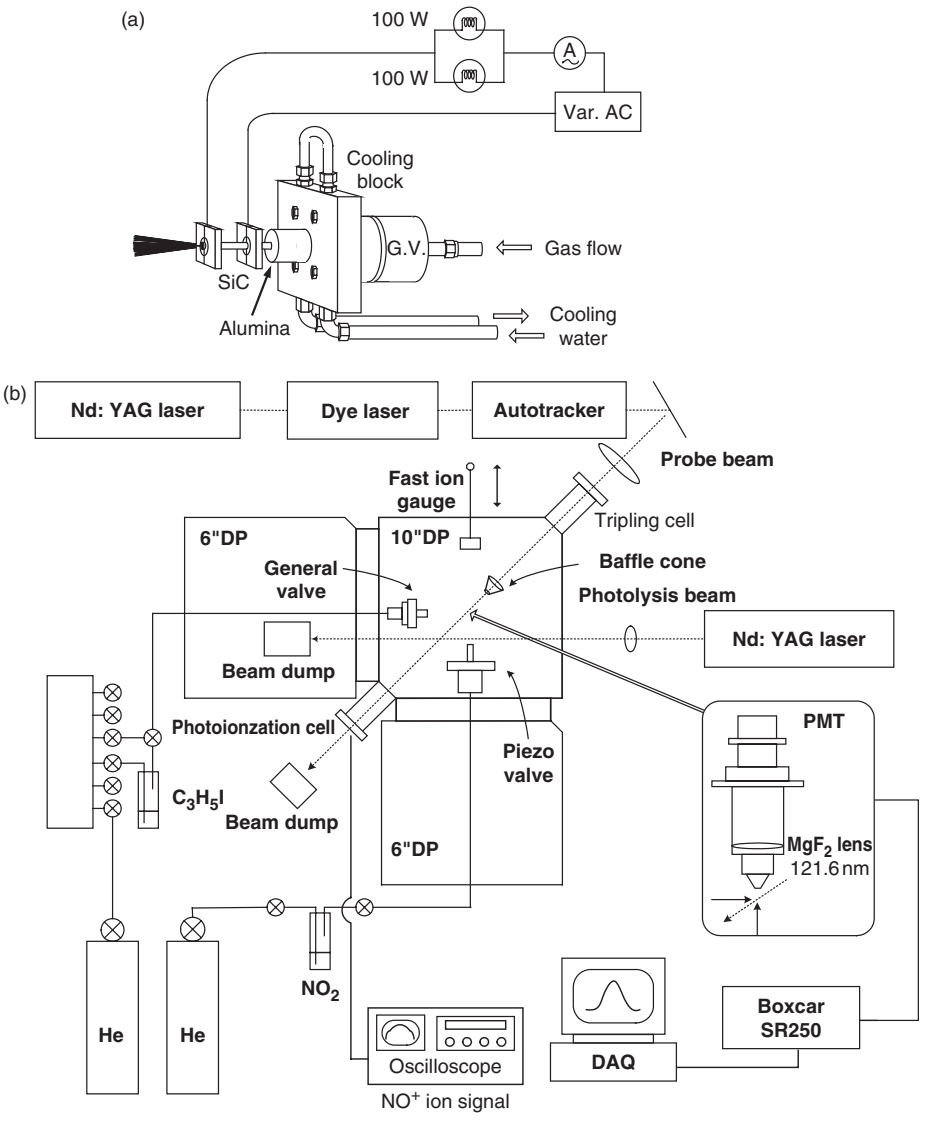

Figure 1. Schematics of (a) the supersonic flash lamp pyrolysis source, and (b) the crossed molecular beam apparatus.

central scattering chamber at right angles. The source and scattering chambers were pumped by two 6-inch (1400 l/s) and one 10-inch (3000 l/s) baffled diffusion pumps, respectively. The average base pressure was maintained at less than 2×10^{-6} torr.

2.1. *Characterization of the molecular beam in the supersonic flash pyrolysis source*

A series of LIF scans was taken to characterize the pyrolysis sources utilized in the experiments. Since our hydrocarbon target radicals did not exhibit fluorescence due to the fast, non-radiative kinetic processes [10], instead, we picked up a precursor

molecule of *n*-butyl nitrite [$CH_3(CH_2)_3ONO$] with a weakly bound and LIF detectable NO component [O–NO bond dissociation energy (BDE) of 42.5 kcal/mol] [18]. After flash decomposition, nitric oxide and atomic iodine were quantitatively generated in a supersonic beam:

$$n\text{-}CH_3(CH_2)_3ONO \rightarrow n\text{-}CH_3(CH_2)_3O + NO$$

The pyrolysis fragment, NO, was detected by LIF spectroscopy and, therefore, acted as a useful probe for understanding the process of radical production.

An *n*-butyl nitrite sample seeded in ultrahigh purity helium (UHP He: 99.999%) at stagnation pressures of 2 and 5 atm was expanded through a pulsed nozzle (0.8-mm diameter, General Valve Co.) into the SiC tube nozzle (1.0-mm diameter, 25-mm length, Carborundum Co.). A SiC tube with a resistively heated length of 10- to 15-mm was attached to the faceplate of the pulsed valve by a water-cooled Al_2O_3 tube, as shown in figure 1(a). The precursor sample was pyrolyzed as the gas flowed through the SiC channel and underwent supersonic expansion into the centre of the scattering chamber. The pressure in the central chamber was maintained at 3×10^{-5} torr with the source operating at a repetition rate of 10 Hz. The pulse width of the supersonic jet was measured by a fast ion gauge based upon the design of Gentry [42]. The LIF detection scheme via the $A^2\Sigma^+ \leftarrow X^2\Pi$ ($\Delta v = 0$) transition of NO was used. The output of the Nd:YAG laser-pumped dye laser system (Continuum Surelite II-10, Spectron SL4000B) operating on Coumarine 450 was frequency-doubled in a BBO crystal mounted on a home-made autotracker and slightly focused by a 50-cm lens into the centre of the supersonic radical beam. To avoid saturation in the fluorescence signal, the probe beam was carefully controlled and maintained at less than several tens of μJ/pulse. The resulting fluorescence from the NO electronic transition was collected through a CaF_2 window and focused with a 20-cm focal length CaF_2 lens onto the PMT (Hamamatsu R166UH) placed in the direction perpendicular to the probe laser beam and the radical beam, as shown figure 1(b). The signal from the PMT was sent to a boxcar averager (Stanford SR250) interfaced to an IBM-PC for display and analysis.

2.2. *Nascent product state distributions from reactive scattering processes*

The ground-state atomic oxygen beam [$O(^3P)$] was generated using NO_2 samples (99.5%, MG Industries) kept at 273 K. The NO_2, which was 12% seeded in UHP He at a stagnation pressure of 2 atm, was expanded through a piezoelectrically actuated pulsed valve (with a 1.0-mm diameter, 40.0-mm long nozzle), and was irradiated by the ca. 30 mJ/pulse of the 355 nm output (6 mm in diameter) of a Nd:YAG laser (Continuum Surelite II-10) near the throat of the supersonic expansion (300 μsec pulse FWHM). $O(^3P)$ was detected through the LIF scheme using the output of the Nd:YAG laser-pumped dye laser system (Continuum Surelite III-10, Lambda Physik Scanmate II). The dye laser beam operating on Coumarine 450 dye was frequency-doubled in a BBO-based autotracker. While atomic oxygen was excited by two-photon absorption at 226 nm ($3p\ ^3P - 2p\ ^3P$), the fluorescence emission was observed at around 845 nm ($3s\ ^3S - 3p\ ^3P$). The resulting fluorescence was collected through a Galileo-type telescope (a CaF_2 window and a 20-cm focal length CaF_2 lens) onto the PMT (Hamamatsu R636-10) placed in the direction perpendicular to the probe and

reactant beams. The observed spin–orbit state distributions of $O(^3P_J)$ showed good agreement with those reported in a previous experiment by Miyawaki *et al.* [43]. No metastable state of atomic oxygen (^1D) was observed under our photolysis conditions, which was confirmed by investigating the reaction with H_2 [21].

Organic hydrocarbon radicals were produced using the supersonic flash pyrolysis source described in the previous section. The precursors, allyl iodide (C_3H_5I), propargyl bromide (C_3H_3Br), and azo-t-butane (C_4H_9–N=N–C_4H_9), which contain weak C–I, C–Br, and N–C bonds with BDEs of 43.5, 62.7 and 43.5 kcal/mol, were chosen to generate the allyl, propargyl, and t-butyl radicals, respectively. Each precursor seeded in UHP He at 2 atm was expanded through the flash pyrolysis source. The precursors underwent complete pyrolysis and then expanded supersonically into the scattering chamber (600 μsec pulse FWHM). The full decomposition of C_3H_5I and C_3H_3Br, was confirmed by applying two-photon LIF spectroscopy to the atomic halogen products. The same pyrolysis behaviour was observed in the time-of-flight experiments, in which the parent precursor ions completely disappeared in the mass spectrum under similar heating conditions [13, 44, 45].

Both reactant beams expanded supersonically into the scattering chamber and were crossed at its centre. Skimmers were not used, due to the small reaction cross-sections of the probed channels. While both beams operated at a repetition rate of 10 Hz, the average background pressure was maintained at less than 1×10^{-4} torr. The overall timing sequence of the two intersecting reactant beams and the probe and photolysis laser beams was controlled with a pulsed delay generator (Stanford DG535) by monitoring the signals from the photodiode and the fast ionization gauge [42].

The nascent rovibrational quantum states of the OH ($X^2\Pi$: $v''=0$, 1, 2) products were examined by high-resolution LIF spectroscopy via the $A^2\Sigma^+ \leftarrow X^2\Pi$ electronic transition in the 306–355 nm region. For $v''=0$ and 1, both the (0, 0) and (1, 1) diagonal bands were recorded, whereas for $v''=2$, the (1, 2) off-diagonal band was recorded due to the J'-dependent predissociation in the $v'=2$ level of the $A^2\Sigma^+$ state [46–49]. Higher vibrational states with $v''>2$ could not be examined on account of the strong fluorescence from NO_2 [50]. The probe beam was produced by the frequency-doubled output of a Nd:YAG laser-pumped tunable dye laser operating on DCM ($\Delta v=0$) and LDS 698 ($\Delta v=-1$) dyes in a BBO-based autotracker. In the diagonal transitions, the probe laser intensity was controlled such that the excitation was saturated by the 3-mm diameter beam at a laser energy of more than 0.2 mJ/pulse. On the other hand, since the Franck–Condon factor of the (1, 2) transition was a factor of ~250 smaller than that of the (0, 0) transition, a higher laser energy of 2 mJ/pulse was used to counterbalance the decreased line strength. Special care was also taken to ensure that the observed fluorescence signals depended linearly upon the probe laser power in the case of the (1, 2) transition. Fluorescence detection was accomplished by means of a combination filter (Melles Griot 03 FIU119, 03 FIU024, 03 FIU006) for diagonal transitions and a single filter (Melles Griot 03 FIU024) for off-diagonal transitions. The minor interfering background was subtracted to obtain the OH signal due solely to the reaction.

The Doppler-broadened line profiles of the atomic hydrogen products were examined by VUV-LIF spectroscopy in the Lyman-α region centred at 121.6 nm.

To obtain a tunable VUV laser beam, the visible laser radiation at around 729.6 nm was first produced by a Nd:YAG laser-pumped dye laser system operating on LDS 750 dye. The dye laser beam (30 mJ/pulse) was then frequency-doubled in a BBO-based autotracker. Afterwards, the 7mJ/pulse of a UV laser beam at 364.8 nm was tightly focused with a 150-mm focal length fused silica lens into the centre of a frequency-tripling cell (25 mm in diameter, 100 mm in length) sealed by a fused silica entrance window and an MgF_2 exit lens (250-mm focal length). The tripling cell in figure 1(b) was filled with a Kr/Ar rare-gas mixture, and the total pressure and its mixing ratio were fine-tuned to accomplish an optimum phase-matching condition at 121.6 nm (10.2 eV) [51–53]. The typical Kr and Ar gas pressures were found to be about 300 and 850 torr, respectively, with a ratio of 1: 2.8. The resultant coherent VUV laser radiation was spatially separated from the fundamental laser beam by an MgF_2 exit lens monochromator. Good separation was ensured by the large variation of the index of refraction with the wavelength at the edge of the lens and the 1-m long travelling distance to the collision centre in the scattering chamber. After passing through the centre of the two intersecting radical beams, the 6-mm diameter VUV laser beam at the collision centre was directed into a photoionization cell (filled with 3% NO in He at 7 torr) [42]. The photocurrent signal from NO (ionization potential of 9.35 eV) was recorded to normalize the LIF signal of the H-atom products with respect to the intensity of the VUV laser intensity.

3. *Ab initio* calculations

Ab initio calculations were carried out to help characterize the nascent product distributions, the reaction mechanism, the major reaction pathways and the kinetic and dynamic characteristics on the lowest doublet potential energy surface. We employed the density functional method and the complete basis set (CBS) model [54–65]. The various geometries of the local minima and transition states along the reaction coordinates were optimized at the hybrid density functional B3LYP levels using the 6–311G(d,p) basis set as the initial guesses. In addition, the vibration frequencies were also computed to characterize the stationary points and the zero-point energy corrections (scaling factor of 0.98). In locating the transition structures, we utilized the synchronous transit-guided quasi-Newton method, by which a starting structure for the optimization of a transition state was automatically generated based upon the connection of the transition structure to the reactants and products. All of the transition states were verified by both the single imaginary frequency and the connections between the designated reactants and products through the intrinsic reaction coordinate calculations. Afterwards, the complete basis set models of CBS-Q and CBS-QB3 were applied to perform more reliable calculations. The estimated heats of formation and reaction enthalpies demonstrated strong agreement with the previously reported experimental values within an accuracy of 2 kcal/mol. Unless otherwise specified, the results presented below are the single-point energies computed at the CBS-QB3 level. All calculations were executed using the Gaussian 98 and 03 systems of programs on an IBM-PC and Compaq Workstation (XP-1000) [66, 67].

4. Experimental and statistical analysis

4.1. *Nascent internal state distributions of OH products*

The spectral assignment of the individual lines in the LIF spectra of the nascent OH ($X\ ^2\Pi$: $v'' = 0, 1, 2$) products was performed by comparing them with the line positions previously reported by Crosswhite and corroborated by spectral simulations [68–71]. The relationship between the observed line intensities and the rotational level populations is in general dependent on the extent of saturation. In our crossed-beam experiment, for $v'' = 0$ and 1, the LIF excitation spectra from both the (0, 0) and (1, 1) diagonal bands were recorded in the saturated regime. For $v'' = 2$, the (1, 2) off-diagonal band was recorded in the unsaturated regime, due to the J'-dependent predissociation in the $v' = 2$ level of the $A^2\Sigma^+$ state. In an $A^2\Sigma^+ \leftarrow X^2\Pi$ electronic transition, as a reasonable approximation, the population $n(v'', N'')$ in the probed, specific rovibrational state can be deduced from the LIF intensity, I_{LIF}, through the following relations:

$$n(v'', N'') = C\, I_{\mathrm{LIF}}[(2J'' + 1) + (2J' + 1)]/(2J' + 1) \quad \text{(saturated)}$$

$$= C' I_{\mathrm{LIF}}(2J'' + 1)/B^{v', J'}_{v'', J''} \cdot P \quad \text{(unsaturated)}$$

where C and C' are the proportionality constants, J'' and J' the total angular momentum quantum numbers in the probed state, $X^2\Pi$, and the upper state, $A^2\Sigma^+$, respectively, and $B^{v', J'}_{v'', J''}$ and P are the Einstein coefficients and the probe laser power, respectively [72–75]. Recall that $J'' = N'' + 1/2$ and $N'' - 1/2$ for the two spin–orbit states, $F_1(^2\Pi_{3/2})$ and $F_2(^2\Pi_{1/2})$, respectively. Assuming a simple Boltzmann distribution, the rotational temperature in each vibrational state can be determined from the logarithmic plot of the population divided by the rotational degeneracy as a function of the rotational energy, that is, $\ln[n/(2J'' + 1)]$ vs. E_{rot}, where the slope corresponds to the rotational temperature.

To obtain the ratio of vibrational partitioning ($P_{v''}$), all of the corresponding rotational populations for the individual branches were summed up, corrected and then compared. Afterwards, corrections such as the Franck–Condon factors [0.90, 0.71 and 0.08 for the (0, 0), (1, 1) and (1, 2) bands, respectively] and vibrational lifetimes (686.0 ns for $v' = 0$ and 748.4 ns for $v' = 1$) were taken into account. Here, the non-radiative predissociation was not considered, since the process was known to occur at $N' > 25$ and $N' > 16$ in the $v' = 0$ and 1 states, respectively [76]. The overall corrections were applied using the following formula,

$$\frac{n_{(v''=1)}}{n_{(v''=0)}} = \frac{I_{R(1-1)} \cdot \tau_0 \cdot FC_{(0-0)}}{I_{R(0-0)} \cdot \tau_1 \cdot FC_{(1-1)}},$$

where I and FC are the intensity and the Franck–Condon factor of each R-branch in the spectrum, respectively, and τ_v is the lifetime of each level in the $v' = 0$ and 1 states.

We derived the relative spin–orbit and Λ-doublet populations from the measured line intensities. For the two fine spin–orbit electronic states, $F_1(^2\Pi_{3/2})$ and $F_2(^2\Pi_{1/2})$,

the low-lying F_1 state was probed by the $P_1(N'')$, $Q_1(N'')$ and $R_1(N'')$ transitions, whereas the F_2 state was probed by the $P_2(N'')$, $Q_2(N'')$ and $R_2(N'')$ transitions. The Λ-doublet propensity represents the preferential orientation of the unpaired π-orbital in the limit of large molecular rotation [Hund's coupling case (b)] [77]. The states labelled $\Pi(A')$ and $\Pi(A'')$ correspond to those with the π^1 orbital parallel and perpendicular to the plane of the rotating diatomic OH product, respectively. For the $A^2\Sigma^+ - X^2\Pi$ excitation, the P or R lines originated from the $\Pi(A')$ states, while the Q lines came from the $\Pi(A'')$ states.

4.2. *Translational energy release*

The symmetric Doppler-broadened spectra of the atomic hydrogen products demonstrated that some fraction of the total available energy was partitioned into the translational energy. The average translational energy of the nascent H atoms in the laboratory frame was determined in order to quantify the energy released. Due to the conservation of momentum and energy weighted by the high mass partitioning factor, the atomic hydrogen would be expected to receive most of the translational energy that was released. The second moment of the laboratory velocity distribution, $\langle \boldsymbol{v}_z^2 \rangle$, can be estimated using the following Doppler-broadened Gaussian profile expression [78–81].

$$\langle \boldsymbol{v}_z^2 \rangle = c^2(\Delta \boldsymbol{v}_D/2\boldsymbol{v}_0)^2/(2\ln 2).$$

Here, v_z represents the velocity component of the absorbing H atoms with respect to the propagation direction of the VUV probe beam, c is the speed of light, v_0 is the central absorption frequency of the atom at rest, and $\Delta\nu_D$ is the full width at half maximum (FWHM). Assuming a spatially isotropic velocity distribution in the laboratory frame, $\langle \boldsymbol{v}_x^2 \rangle = \langle \boldsymbol{v}_y^2 \rangle = \langle \boldsymbol{v}_z^2 \rangle$, the average translational energy of the H atoms, $\langle E_T^{lab}(H) \rangle$, can be directly calculated from the equation $\langle E_T^{lab}(H) \rangle = [3m(H)/2]\ \langle \boldsymbol{v}_z^2 \rangle$.

Since, for the centre-of-mass (COM) motion of the O + RH system, the average kinetic energy in the laboratory frame, $\langle E_T^{lab}(O - RH) \rangle$, is given by

$$\langle E_T^{lab}(O - RH) \rangle = [m(O)\langle E_T^{lab}(O) \rangle + m(RH)\langle E_T^{lab}(RH) \rangle]/m(RH - O),$$

the average translational energy of the H + RO products in the COM frame, $\langle E_T^{com} \rangle$, can be estimated from $\langle E_T^{lab}(H) \rangle$ and the following expression:

$$\langle E_T^{com} \rangle = [m(RH - O)/m(RO)][\langle E_T^{lab}(H) \rangle - m(H)\langle E_T^{lab}(RH - O) \rangle/m(RH - O)].$$

4.3. *Statistical analysis*

It is worthwhile obtaining the energy-specific rate constants for the unimolecular decomposition pathways of the energized intermediates using statistical RRKM theory, and making a comparison of these constants with the experimental results and *ab initio* predictions [82–85]. The RRKM rate constants obtained from the microcanonical

transition state theory can be calculated using the following equation expressed as an explicit function of the total available internal energy, E_{avl}, of the intermediate,

$$k_i(E_{avl}) = \frac{G_i(E_{avl} - E_i^{\neq})}{hN(E_{avl})},$$

where h is the Planck constant, $E_i^{\neq}$ is the corresponding barrier height for the particular channel, i, $G_i(E_{avl} - E_i^{\neq})$ is the sum of states for the transition state at energy $E_{avl} - E_i^{\neq}$, and $N(E_{avl})$ is the density of states for the intermediate at energy E_{avl}. The available energy, E_{avl}, is given by the following expression:

$$E_{avl} = E_{com} + E_{int}(\mathrm{RH}) - \Delta H_{rxn},$$

where E_{com} is the centre-of-mass collision energy and is estimated to be 6.4, 6.1 and 7.9 kcal/mol for the O(^{3}P)-allyl, -propargyl, and -t-butyl systems, respectively. E_{int}(RH) is the internal energy of the hydrocarbon radical, and is negligibly small. ΔH_{rxn} is the reaction enthalpy for the formation of the intermediates of interest. The principal moments of inertia and vibrational frequencies necessary to determine $G_i(E_{avl} - E_i^{\neq})$ and $N(E_{avl})$ are obtained from the *ab initio* calculations.

The observed nascent distributions were compared to those predicted by the statistical theory, in order to examine the dynamic characteristics of the OH products. The simplest statistical approach which can be used to calculate the product state distributions for the decomposing energized intermediate in an exothermic reaction is known to be the *prior* calculations, in which all of the allowed quantum states of the products are assumed to be equally accessible and the distributions are determined by calculating the available volumes in the phase space of the two fragments [84]. Since the masses of the reactants and products differ by only 1 amu in the H-atom transfer reaction, the angular momentum constraints are considered relatively unimportant and, consequently, the prior distributions are constrained only by energy conservation. The prior distribution for OH in a specific rovibrational state, $n^{\circ}(v'', J'')$, can be determined by using the following expression:

$$n^{\circ}(\upsilon'', J'') \propto (2J'' + 1)n(E_V) \sum_V \rho(E_v)(E_{avl} - E_J - E_V - E_v)^2.$$

Here, $(2J'' + 1)$ is the rotational degeneracy of the diatomic OH fragment, and $n(E_V)$ is the degeneracy of the OH vibrational states, which is unity for a diatomic molecule. The summation was calculated through integrations over the 3D translational density of states using the reduced mass of R and OH, and the classical rotational density of states of the R-product. The vibrational density of states was assessed using the direct count of states. The only quantities required to determine $n^{\circ}(v'',J'')$ were the vibrational frequencies used for calculating $\rho(E_v)$, which were obtained from the *ab initio* calculations. Furthermore, the estimated rotational distributions, which appeared Boltzmann-like over a broad range, were therefore used to allocate

the temperatures. Since the extreme limits corresponding to the low- and high-N'' regions were susceptible to possible relaxation and the thermal distribution of the reactant energies, respectively, only those states belonging to the interval between the low and high rotational states (extending over a region corresponding to >90% of the populated levels) were employed to obtain the rotational temperatures. The prior partitioning ratio of vibrational states is obtained by summing over the entire rotational prior distribution for each vibrational level.

A rotational surprisal analysis was also performed to estimate the extent of the deviation from the statistical distribution [1]. The surprisal,

$$I(f_r/f_v) = -\ln[n(v'', J'')/n^{o}(v'', J'')]$$

is plotted as a function of the rotational fraction of the available energy, $g_R = f_r/(1 - f_v)$. Here f_r and f_v are the fractions of the rotational and vibrational energies of the OH product, respectively.

5. Radical–radical reaction dynamics

5.1. *Characteristics of the molecular beam in the supersonic flash pyrolysis source*

A systematic comparison of the rotational population analysis as a function of the heating power was conducted with and without a flash pyrolysis source for the same sample beams consisting of 3% NO in He (table 1).

As the SiC nozzle is heated, the sample gas mixture absorbs the heat energy from the hot cylindrical wall through thermalizing collisions. Under the typical experimental conditions, the SiC wall temperature was estimated to be as high as 1500 K. Since the most important temperature is the internal temperature of the sample molecules in the gas flow, the dynamics of the heat transfer from wall to sample is believed to determine the efficiency for the absorption of heat and the processes of decomposition. Barney Ellison *et al.* performed approximate calculations for a 1% N_2O/He flow at a wall temperature of 1500 K and determined that the gas absorbs a significant amount

Table 1. Rotational temperatures of NO at different heating powers and backing pressures.

			Rotational temperature (K)	
Precursor	Backing pressure (atm)	SiC tube heating (W)	$F_1(R_1 + Q_{21})$	$F_2(Q_2 + R_{12})$
NO	2	w/o SiC	6	0
		0	10	0
		9.5	100	140
		20	100	160
		32	120	175
	5	20	80	140
n-C_4H_9ONO	2	20	170	210
	5	20	85	170
		30	105	170

(about 80%) of the heat from the tube wall during a short passage time of 20 μsec and that the internal temperature reaches around 800 K [86].

The series of experimental LIF spectra shown as a function of the heating power in figure 2 exhibit just such an internal excitation of the jet, as is borne out by the observation of the spectral transitions from the electronically excited $X^2\Pi_{3/2}$ (F_2) state and the broad rotational population distribution in each spin–orbit state. In particular, the P_{11} band head of $X^2\Pi_{1/2}$ (F_1) and the $P_{22}+Q_{12}$ band head of $^2\Pi_{3/2}$ are sensitive measures of the rotational excitations. A gradual increase in the height of each band

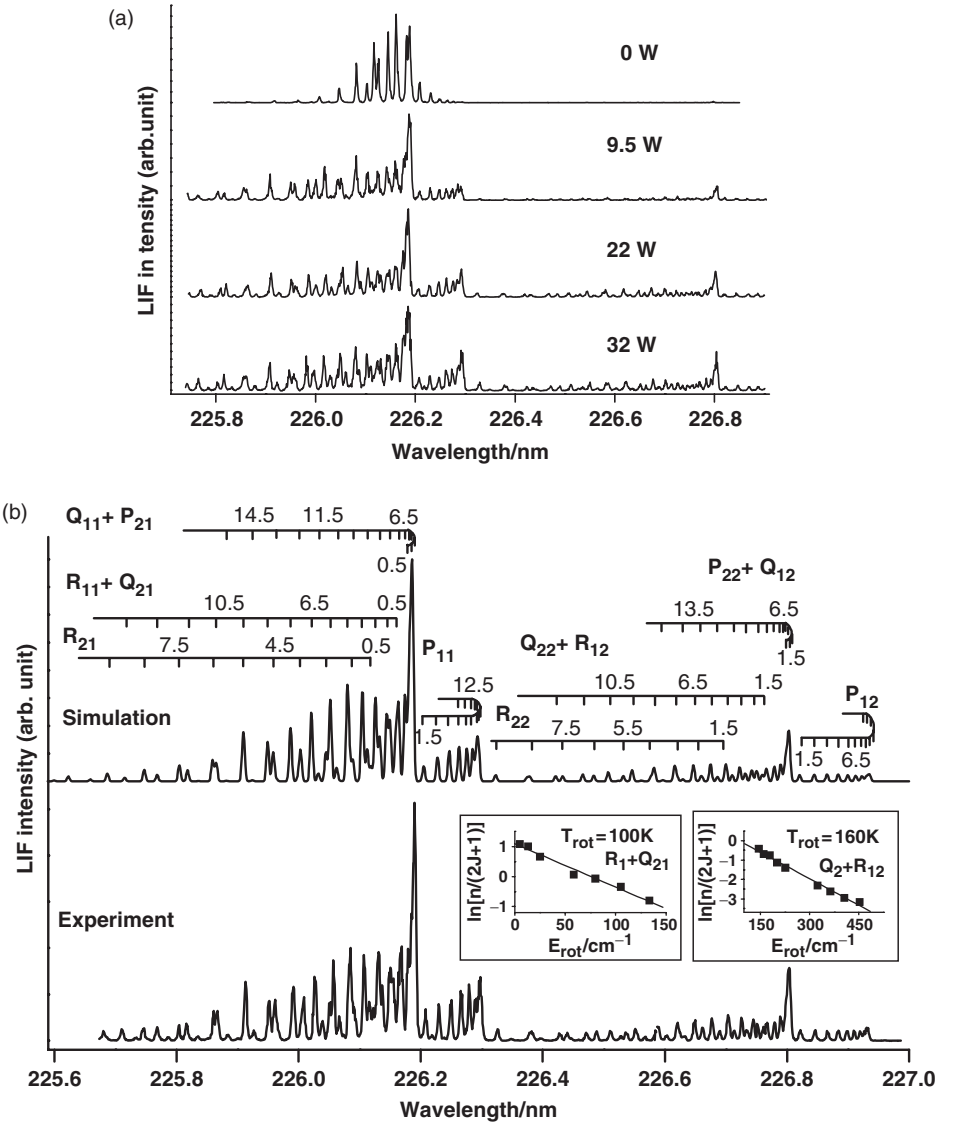

Figure 2. (a) Dependence of the NO [$A^2\Sigma^+ \leftarrow X^2\Pi$ ($\Delta v = 0$)] LIF spectra on the pyrolysis heating power. (b) Experimental and simulated NO spectra at 20 W.

head was observed as the heating power was increased. In determining the rotational temperatures, the population distribution in the excited $^2\Pi_{3/2}$ state was found to be different from that in the ground $^2\Pi_{1/2}$ state. Table 1 lists the estimates obtained for the rotational temperatures in each electronic state at three different heating powers, and shows the higher rotational temperatures of the excited $^2\Pi_{3/2}$ state. The spectral simulation using two different rotational temperatures at a heating power of 20 W shows good agreement with the experimental spectrum, as shown in figure 2(b). The observed non-equilibrium between the two spin–orbit $^2\Pi_{1/2}$ and $^2\Pi_{3/2}$ states can be explained by their different collision-induced energy transfer rates [87]. For NO/He expansion, the energy transfer rate from one spin–orbit manifold to the other is known to be about ten times smaller than that within the same manifold. As the jet expansion proceeds, therefore, the lower J states of the $^2\Pi_{3/2}$ states are quite inefficient at transferring energy to the rotational states of the $^2\Pi_{1/2}$ states, leading to a lack of local equilibrium between the two spin–orbit states. The extent of rotational cooling was also examined by changing the expansion parameter ($P_s \cdot d$), where P_s is the nozzle stagnation pressure and d is the nozzle diameter. It is well known that the internal temperature of the supersonic molecular beam decreases as the expansion parameter is increased [88, 89]. As can be seen in table 1, at a heating power of 20 W, the rotational temperatures in both spin–orbit states decrease by 20 K when the stagnation pressure is increased from 2 to 5 atm.

In the case of *n*-butyl nitrite shown in figure 3, the pyrolysis is initiated by the breaking of the weakest bond of RO–NO (BDE = 42.5 kcal/mol), resulting in the generation of nitric oxide and butoxy radicals. To obtain the extent of fragmentation

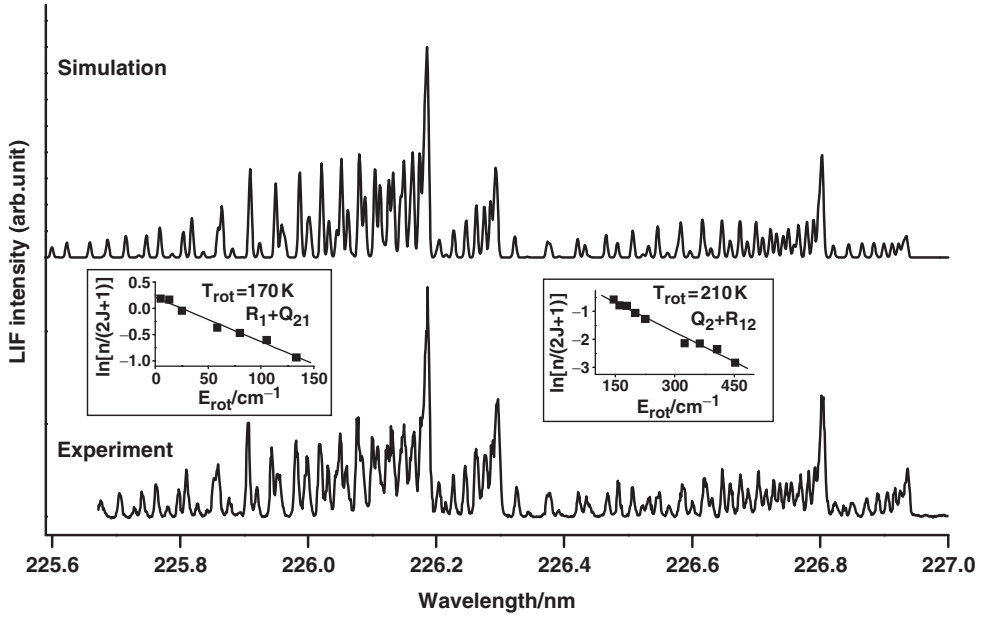

Figure 3. Experimental and simulated spectra of the fragment NO [$A^2\Sigma^+ \leftarrow X^2\Pi$ ($\Delta v = 0$)] resulting from the flash pyrolysis of *n*-butyl nitrite at 20 W.

of the precursor under our experimental conditions, we examined the unimolecular reaction kinetics of *n*-butyl nitrite. Batt and coworkers studied the decomposition kinetics of a series of alkyl nitrates in a static system and obtained the rate constant for *n*-butyl nitrate: $k_d(T) = 1 \times 10^{16} \exp[-41.8\,\text{kcal/mol/(RT)}]$ [90, 91]. If we assume that the internal temperature of *n*-butyl nitrite attains 800 K during the passage (residence) time of 20 μ sec, then it can be inferred that the unimolecular reaction proceeds through the following equation

$$[\text{P}] = [\text{P}]_\text{o} \exp[-k_d(T)t]$$

and leads to its decomposition such that the initial nitrite precursor $[\text{P}]_\text{o}$ is completely pyrolyzed into NO and *n*-butoxy radicals.

Figure 3 displays the observed spectrum of the pyrolysis product NO at a heating power of 20 W. In this experiment, no LIF signal was detected without heating, indicating that the NO spectrum was the direct outcome of the precursor pyrolysis. The intensity of the signal and the spectral distribution increased as the heating power was increased. The rotational temperatures in the two electronic $^2\Pi_{1/2}$ and $^2\Pi_{3/2}$ states were found to be different, as in the case of the 3% NO/He beam, and decreased as the expansion parameter was increased (table 1). A similar temperature in the $^2\Pi_{1/2}$ state was also reported in the pyrolysis experiments of ethyl nitrite using FT-IR spectroscopy. Our pyrolysis experiment presents the characterization of the incomplete equilibrium between the two spin–orbit states of the radical products generated in the flash pyrolysis of precursor molecules.

5.2. *Reaction dynamics of O(^{3}P) with C_3H_5*

5.2.1. *Ab initio* potential energy surface: addition vs. abstraction. The detailed theoretical investigations of the reactive $\text{O}(^3\text{P}) + \text{C}_3\text{H}_5$ scattering processes were described elsewhere [29] and here only a brief explanation of the pathways leading to the formation of the H and OH products is presented. Figure 4 shows the schematic diagrams of the reaction pathways on the lowest doublet potential energy surface using the CBS-QB3 level of *ab initio* theory. In the case of addition processes, as atomic oxygen attacks the allyl radical, several energy-rich addition intermediates are formed along the entrance pathways, due to the long-range attractive interactions between the two reactant radical species. The addition of $\text{O}(^3\text{P})$ to the terminal carbon(3) forms an intermediate species, $\text{CH}_2\text{CHCH}_2\text{O}$ (denoted as INT1), whereas its addition to the central(2) and terminal(3) carbons forms an O-atom bridged intermediate INT2 (not shown), lying 0.9 kcal/mol above INT1. For INT2, the calculation predicts fast conversion to INT1 via the breakage of the C(2)–O bond (a very low barrier height of only 3.7 kcal/mol). Another intermediate, INT3, which has 7.5 kcal/mol more exothermicity than INT1, is a three-membered ring of carbon atoms. All of the addition association processes are calculated to be barrierless as a result of the bond formation between the two reactive radical species. Furthermore, the plentiful internal energy of the association intermediates would be expected to be available for subsequent isomerization or decomposition steps, leading to the formation of a variety of products.

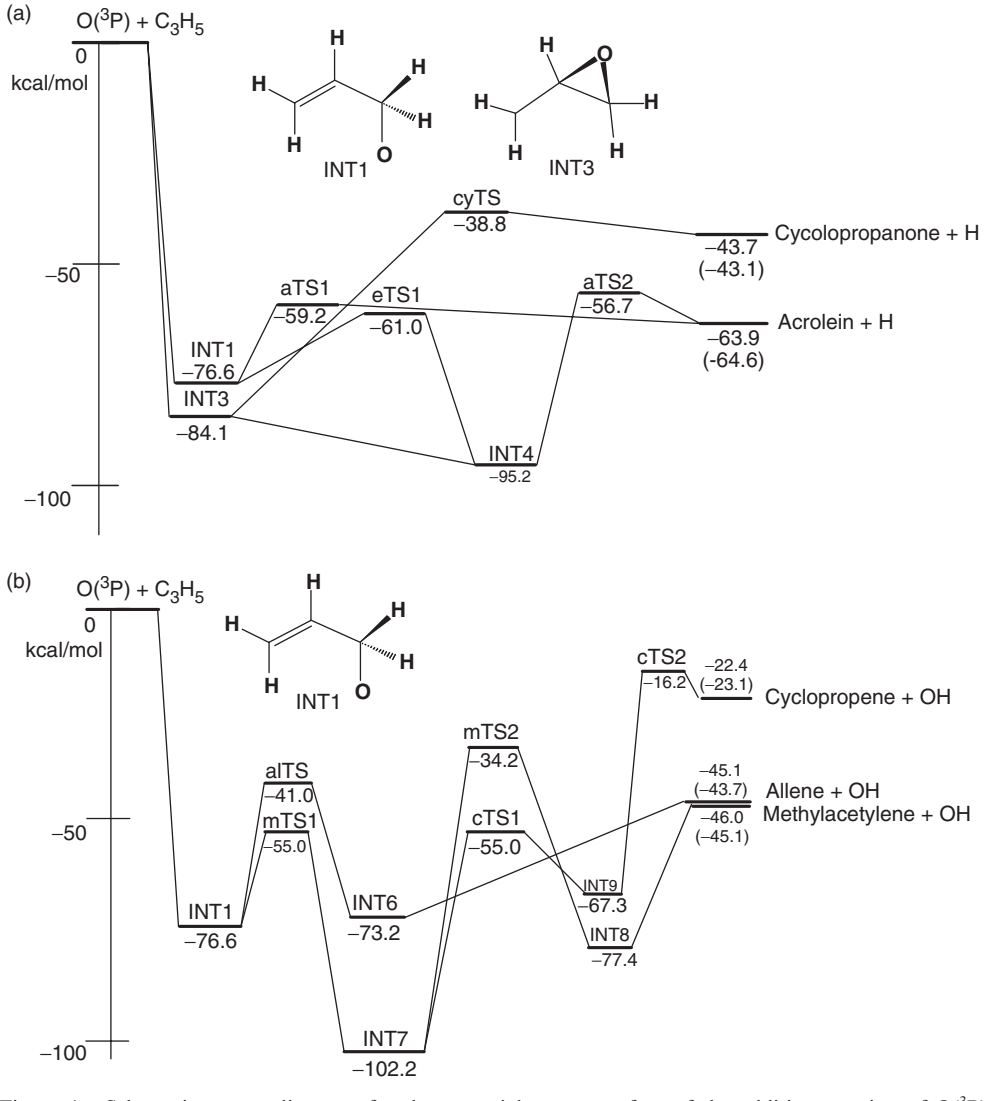

Figure 4. Schematic energy diagrams for the potential energy surface of the addition reaction of $O(^3P)$ with an allyl radical at the CBS-QB3 level of the theory. The values in parentheses denote the experimental values (kcal/mol). (a) Pathways to the formation of $H(^2S) + C_3H_4O$ and (b) pathways to the formation of $OH + C_3H_4$. The optimized geometries of the various species are shown in the Supplementary Materials.

In the formation of the atomic hydrogen product, the polyatomic counterpart, C_3H_4O, is known to have two different isomers, acrolein and cyclopropanone. For the highly energized INT1, two pathways to the formation of H + acrolein are predicted to compete, as shown in figure 4(a). The relatively facile channel is the direct C(3)–H bond cleavage through the transition state, aTS1. The optimized geometry of aTS1 is calculated to be close to that of acrolein, indicating that aTS1 shows the feature of a product-like late barrier. Another competing channel of INT1 producing

the same products first involves the three-membered transition state eTS1 through the [3,2]-H-migration leading to the aldehyde radical intermediate, INT4 (CH_2CH_2CHO). The corresponding barrier height is estimated to be only 15.6 kcal/mol, which is slightly lower than the typically reported range of 20–40 kcal/mol for the H-atom migration process. Afterwards, INT4 undergoes a direct C(2)–H bond cleavage through the transition state, aTS2, overcoming a barrier height of 38.5 kcal/mol. The formation of H + cyclopropanone might be a second feasible reaction pathway of INT3 through the direct segregation of atomic hydrogen from the O-atom-bonded carbon of cyTS. The most facile pathway to explain the observed H-atom products is believed to be the INT1 channel to the H + acrolein products via aTS1. The INT1 pathway through the low-barrier transition state, aTS1, involves the direct single-step cleavage. The predicted acrolein pathway is consistent with the previous gas-phase bulk experiment performed by Gutman *et al.*, in which only the acrolein + H channel was observed at the detectable levels of their study [40].

The formation of $C_3H_4 + OH$ is another competing channel of INT1 and was first observed in our crossed-beam experiment. The counterpart of the probed OH product, C_3H_4, is known to be one of the three different isomers shown below:

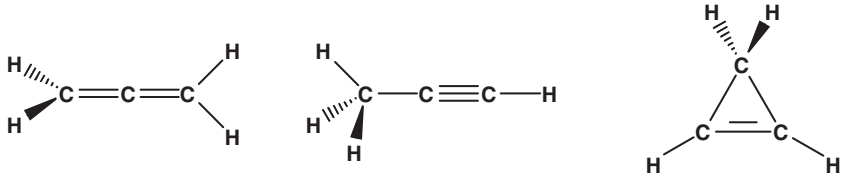

While the allene and methylacetylene channels show nearly the same exothermicities of −45.1 and −46.0 kcal/mol, respectively, the cyclopropene channel is calculated to be less exothermic (−22.4 kcal/mol). In the case of the addition process, the most likely of the three reaction channels to yield the OH product is the allene channel. The pathway to allene involves the migration of the H-atom from the central carbon(2) of the energy-rich INT1 to the oxygen atom, followed by direct decomposition to allene + OH. The corresponding barrier height of the initial migration step is calculated to be 35.6 kcal/mol. For the methylacetylene and cyclopropene channels, INT1 might first undergo H-migration from the carbon(3) to the oxygen atom to form $CH_2CHCHOH$, by overcoming the low barrier of 21.6 kcal/mol. Then, $CH_2CHCHOH$ might undergo either a second [1,2]-H-migration followed by direct bond rupture to form methylacetylene + OH, or ring closure followed by direct decomposition to produce cyclopropene + OH. In comparison to the allene pathway, significantly higher barriers of 68.0 and 47.2 kcal/mol have to be overcome in the methylacetylene and cyclopropene channels, respectively, which also require one additional step to yield the products.

However, the dominant process leading to the formation of OH products is the direct abstraction process. The abstraction mechanism is commonly observed in the investigation of the reaction dynamics for $O(^3P)$ with closed-shell hydrocarbon molecules. In the previous systematic studies conducted by Andresen and Luntz, the exothermic reactions for $O(^3P) + RH \rightarrow R + OH$ were found to proceed via an H-atom

abstraction mechanism on the lowest triplet surface, which correlates with the OH and hydrocarbon radical R [92]. The probed OH product was non-statistically generated with a considerable fraction of the available energy being channelled into the vibrational energy of the product, as well as a small amount of rotational excitation, and the extent of the vibrational excitation was increased across the series of primary to tertiary hydrocarbons. Such H-atom transfer reactions have been qualitatively interpreted in terms of a simple triatomic abstraction model assuming a collinear transition state, O–H–R. Since the process is very immediate, after passing through the transition-state region, the incomplete energy randomization among the products leads to a non-statistical outcome in the energy distributions of the OH product.

Figure 5 shows the *ab initio* potential energy diagram for the direct H-atom abstraction reaction for the $O(^3P) + RH \rightarrow R + OH$ systems. This diagram shows that as the reaction exothermicity increases, the attractive character in the entrance channel is gradually enhanced for the series of primary, secondary, and tertiary hydrocarbons as a result of the decreasing barrier to H-atom abstraction. Especially, the entrance barrier in the case of O + allyl is estimated to be negligible. This calculation is quite consistent with the so-called Hammond postulate which states that for exothermic reactions, a low activation barrier implies the structural similarity of the reactant and transition states [3]. For the highly exothermic O-allyl system, it would be expected for the transition state to be an early barrier in the reactant channel and the barrier height to be significantly smaller than those for the less exothermic O + RH systems. Such an early barrier in the potential energy surface can be ascribed to the large

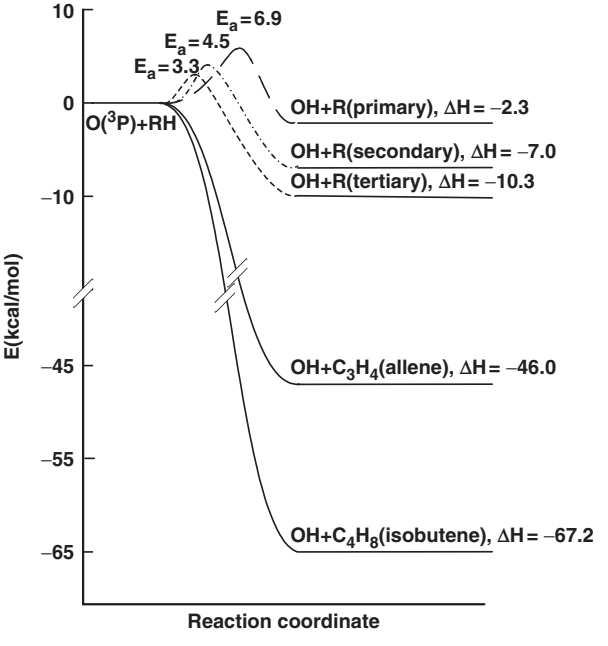

Figure 5. The energy profile for the H-atom abstraction processes in the reactions of $O(^3P)$ with a series of saturated hydrocarbon molecules and allyl and t-butyl radicals.

reaction cross-section, which results from the strong long-range interactions between the two reactive radical species. Therefore, for the reaction $O(^3P) + C_3H_5 \rightarrow C_3H_4 + OH$, the direct, barrierless abstraction process involving a collinear transition state should be taken into account as a competing channel, in order to understand the microscopic mechanism.

The most facile H-atom abstraction process is predicted to be the abstraction from the central carbon of allyl, due to the small bond dissociation energy. While the H-atom abstraction from the central carbon is calculated to involve only 57.6 kcal/mol, the abstraction from one of the two terminal carbons requires 119.1 kcal/mol. In addition, after the H-atom abstraction from the central carbon, a stable allene product is formed. However, the abstraction from the terminal carbon necessitates another unfavourable isomerization step to produce methylacetylene or cyclopropene. The process described above is also quite consistent with a recent photodissociation study of the allyl radical, in which the dominant H-atom-loss pathway was found to be the dissociation of the middle C–H bond, leading to the formation of stable allene [9, 12, 44].

After taking into account the reaction enthalpy, barrier height and the number of intermediates involved along the reaction coordinate, the major pathway for the $O(^3P) + C_3H_5$ reaction is found to be the formation of acrolein + H, and it is highly probable that the counterpart species of the OH product observed in this study is allene generated via competing abstraction and addition mechanisms.

5.2.2. $O(^3P) + C_3H_5 \rightarrow C_3H_4 + OH$. Figure 6 displays a typical LIF spectrum of the OH ($X\ ^2\Pi$: $v'' = 0, 1$) product. The OH spectrum in figure 6(b) only in the low-N'' region was ascribed to the photolysis of the HONO impurity which was always present in the NO_2 sample. The minor interfering background signal was subtracted to obtain the spectrum due solely to the reaction. Furthermore, we attempted to confirm the absence of the metastable $O(^1D)$ species by investigating the reaction with H_2. Due to the large cross-section and high exothermicity of the reaction of $O(^1D)$ with H_2 only the metastable $O(^1D)$ species, if it exists, would generate the OH signal in *both* the low- and high-N'' regions [93, 94]. The spectrum in figure 6(c), which is very nearly the same as that in figure 6(b), suggested that $O(^3P)$ was solely responsible for the observed OH signal.

Figure 7(a) shows the logarithmic plots of the population divided by the rotational degeneracy as a function of the rotational energy. Considerable rotational excitations up to $N'' = 19$ for $v'' = 0$ and $N'' = 16$ for $v'' = 1$ were observed. The population analysis evidently displays bimodal features in each vibrational state. One regime corresponds to the distribution of only the lower N'' rotational states, while the other corresponds to a broader distribution of the higher N'' rotational states. This feature is more obviously exhibited in the $v'' = 0$ state, where the fraction of rotational energy in the available energy of the system is higher.

The estimates of the rotational temperatures, vibrational partitioning, spin–orbit, and Λ-doublet state populations are tabulated in table 2. Substantial vibrational excitation is manifested in the (1,1) region of the $A\ ^2\Sigma^+ - X^2\Pi$ transition of the spectrum, and the averaged partitioning ratios for the low- and high-N'' components were found to be almost the same in the two spin–orbit states. The averaged ratios

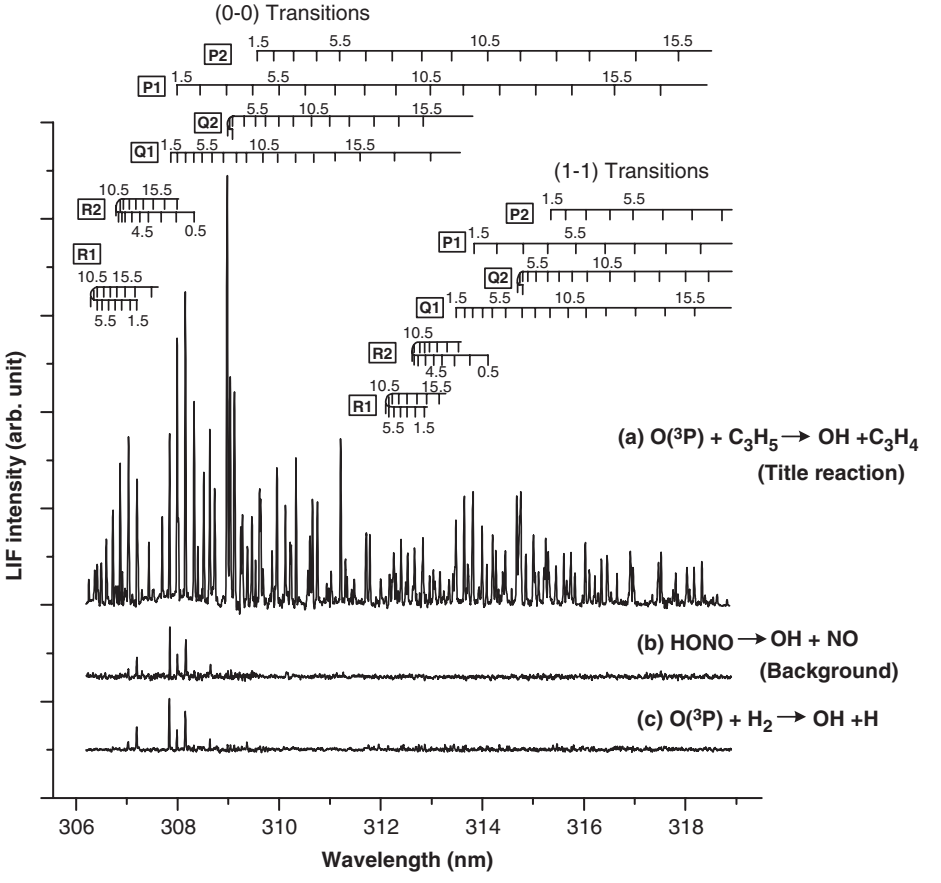

Figure 6. The LIF spectrum in the 0–0 and 1–1 band regions of the nascent OH ($A^2\Sigma^+ - X^2\Pi$) produced in the reaction of $O(^3P)$ with an allyl radical.

of the two spin–orbit states, $F_1N''/F_2(N''+1)$ and $\Pi(A')/\Pi(A'')$, are summarized in table 2 and figure 7. No spin–orbit or Λ-doublet preferences were observed in any vibrational state. To better characterize the experimental distributions, the statistical prior and surprisal theories were applied. The prior calculations predicted much higher rotational temperatures and a smaller vibrational partitioning, as listed in table 2. The rotational surprisal in figure 8 fit very poorly, except for the large negative slope in the low-N'' regime, signifying that the low rotational components are highly populated as compared to the statistical distributions.

The bimodal and non-statistical nascent distributions observed in our $O(^3P)$ + allyl reactive scattering processes are quite unusual for the reactions of atomic oxygen. The common reaction mechanism reported in previous studies of the reactions of $O(^3P)$ with saturated hydrocarbons was expressed in terms of the unimodal distributions of the vibrationally hot and rotationally cold $OH(X\,^2\Pi)$, together with a slight preference for the lower spin–orbit state $F_1(^2\Pi_{3/2})$ over the $F_2(^2\Pi_{1/2})$ state [95]. As shown in the Boltzmann plots and normalized rotational populations in figure 7, however, the distinctive bimodal distributions are clearly demonstrated and, therefore,

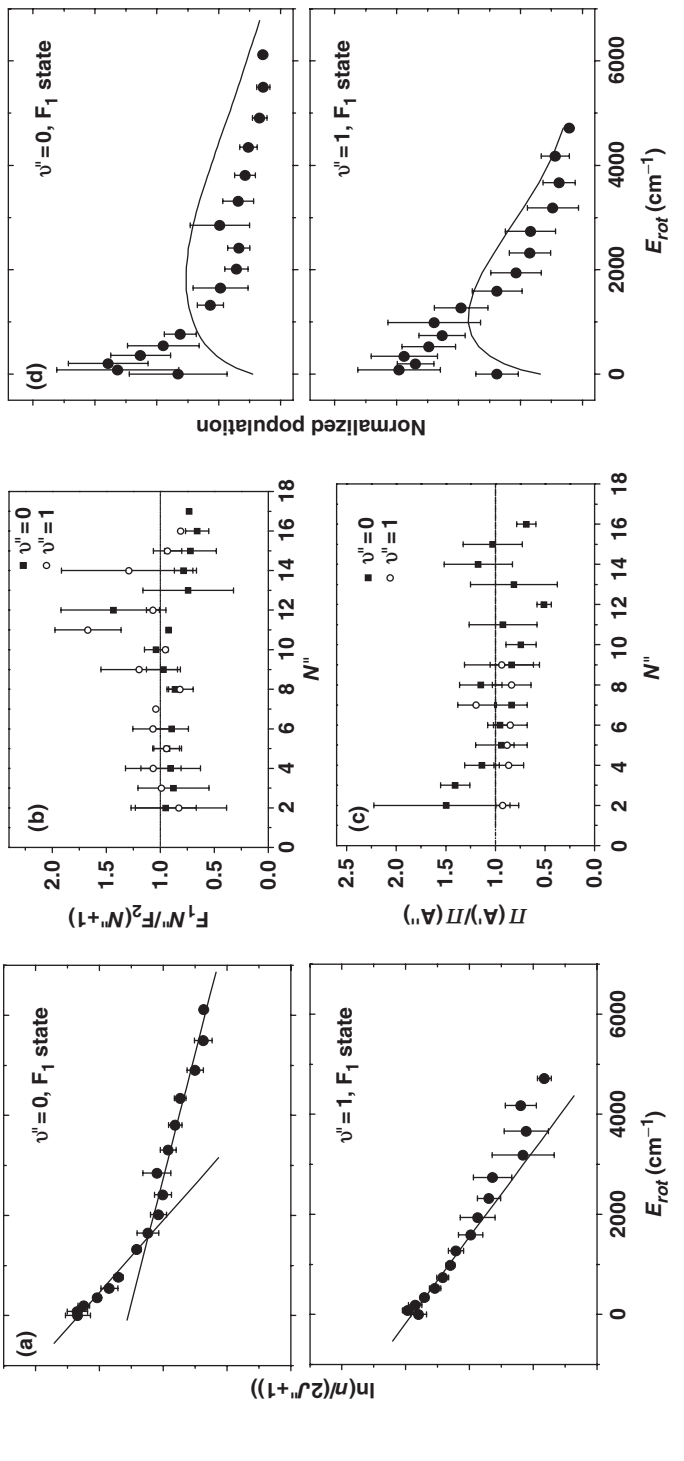

Figure 7. (a) Boltzmann plots of the nascent OH distributions as a function of the rotational energy for the F_1 states of $v'' = 0$ and 1. (b) Spin–orbit state population ratios for $v'' = 0$ and 1. (c) Λ-doublet population ratios for $v'' = 0$ and 1. (d) Normalized rotational populations (filled circles) with statistical prior (—) plots.

Table 2. Summary of experimental and prior results for the OH rotational temperatures, spin–orbit, and Λ-doublet state populations, and vibrational partitioning ratios.

			Rotational temperatures (K)			Spin–orbit state	Λ-doublet	$P\nu''/P\nu''=0$	
			Low–N''	High-N''	Prior	($F_1N''/F_2(N''+1)$)	[$\Pi(A')/\Pi(A'')$]	Experiment	Prior
$O(^3P)+C_3H_5$	$\nu''=0$	F_1	1040	3580	4800	0.90 ± 0.16	0.98 ± 0.26	1	1
		F_2	970	3380	4710				
	$\nu''=1$	F_1	1160	–	2920	1.05 ± 0.18	0.93 ± 0.12	0.75 ± 0.11 (low–N'')	0.33
		F_2	1270	–	2840				
$O(^3P)+C_3H_3$	$\nu''=0$	F_1	480	3140	1160	1.09 ± 0.34	0.60 ± 0.28	–	–
		F_2	390	3840	1170				
$O(^3P)+t\text{-}C_4H_9$	$\nu''=0$	F_1	1310	3830	1710	1.11 ± 0.33	0.85 ± 0.39	1	1
		F_2	1290	3750	1690				
	$\nu''=1$	F_1	1610	–	1650	1.23 ± 0.39	0.98 ± 0.32	1.17 ± 0.24	0.05
		F_2	1690	–	1500				
	$\nu''=2$	F_1	1530	–	1400	1.27 ± 0.32	–	1.40 ± 0.11	0.003
		F_2	1450	–	1270				

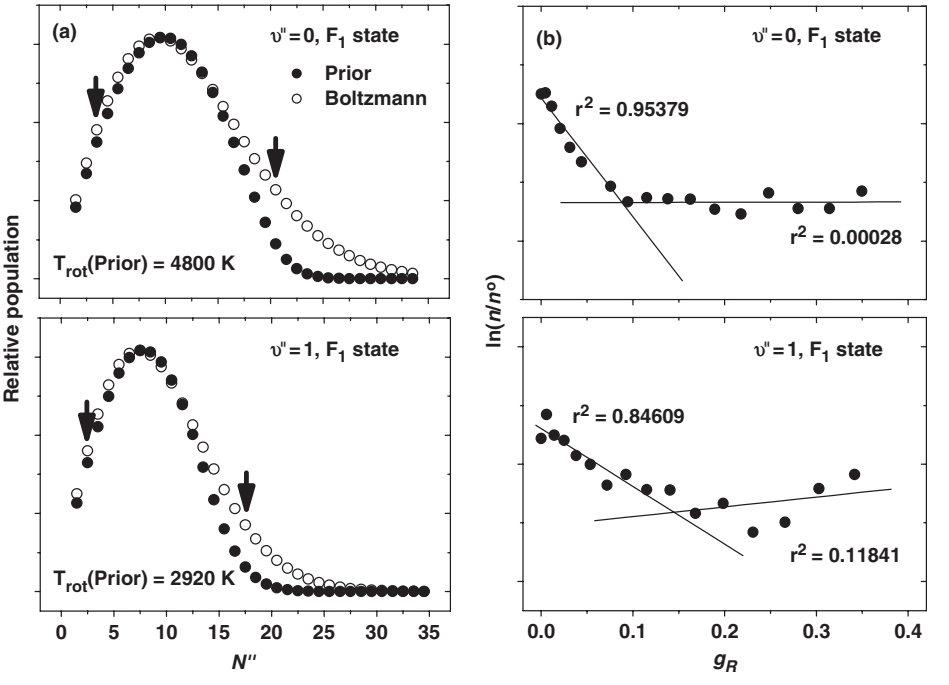

Figure 8. (a) Prior (filled circles) and Boltzmann (open circles) distributions obtained using an average available energy of 51.5 kcal/mol. The arrows indicate the intervals used to assign the rotational temperatures. (b) Rotational surprisal plots for the nascent OH produced in the reaction of $O(^3P)$ with the allyl radical.

implicitly suggest that some competing dynamical channels are involved. On the basis of the *ab initio* calculations, the results might be rationalized by a direct abstraction process and an indirect short-lived addition-complex forming process.

The highly populated low-N'' components with significant vibrational excitation might be ascribed to the former abstraction mechanism. The facile abstraction process is predicted to be the H-atom abstraction from the middle carbon due to the small bond dissociation energy, as described in the previous section. The newly formed OH product was generated characteristically with a considerable fraction of the available energy being channelled into the product vibrational energy, as well as a small amount of rotational excitation. Since the process was very immediate, after passing through the collision transition-state region, the incomplete energy randomization among the products led to the non-statistical outcome of the OH product distributions. Furthermore, although the detailed adiabatic correlation diagram for the reaction including all orientations of the $O(^3P)$ approach and spin–orbit levels is unavailable, it is not surprising that both spin–orbit states are non-selectively produced during such extremely reactive scattering processes. In addition, since the Λ-doublet notation and propensity are significantly related to the directed orbitals in the limit of high-N'', the reaction is likely to generate both Λ-doublet components equally, without any preferential population of either Λ-doublet states, as shown in figure 7. Such a deficiency in the dynamic propensity is in good agreement with the previous observations of OH produced in the reactions of $O(^3P)$ with alkanes [92].

In contrast, the extraordinarily hot rotational distribution observed in this work indicates that some fraction of the reactants is sampled to proceed through the formation of an addition complex such as INT1, as shown in figure 4. The rotational temperatures inferred from the high-N'' components were found to be significantly higher than those from the low-N'' components, and to be rather closer to the prior temperatures, as indicated in table 2. However, such an intermediate was not expected to live long enough to allow the available energy to be statistically partitioned among all the degrees of freedom prior to its dissociation, as evidently manifested in the comparison of the experimental results with the prior analysis. The fast and random decomposition behaviour of the short-lived, energy-rich intermediate was also quite consistent with the equally populated Λ-doublet components. In the case of the channel to allene, the intermediate generated through the H-atom migration from INT1 in figure 4 is calculated to possess a bent geometry with a C–O–H angle of 107.2°. Of course, the intermediate is not expected to assume such a specific angle, due to its large energy content, and instead is likely to behave as a floppy species. Moreover, it is possible that the large impact parameters covering a wide range of approach orientations would cause numerous trajectories to become accessible, leading to the formation of various conformations. When such bent intermediates fall apart so as to generate fragment products, a torque is obviously imparted to the fragments, which manifests itself as rotational excitation in the course of the reaction. The non-preferentially populated Λ-doublet components in the observed rotational excitation for the high-N'' components indicate that the in- and out-of-plane torques within a COH plane act nearly equally during the fast decomposition. Therefore, there would be no dynamic propensity to populate one state over the other.

To the best of our knowledge, there are no other gas-phase studies of $O(^3P)$ with hydrocarbon radicals performed in a crossed-beam configuration with which our results can be compared. Similar bimodal distributions have been observed in the exothermic reactions of electronically excited atomic oxygen $O(^1D)$ with saturated hydrocarbon reactions [49, 96–101]. Wiesenfeld *et al.* found that the major high-N'' regime (about 80% of the relative yields) was ascribed to the short-lived insertion process and adequately described by the linear surprisal. It was also possible to deduce the population of the low-N'' regime by subtracting the prior distribution scaled by the surprisal parameter from the nascent distribution. They found that the minor low-N'' regime was well characterized by the Boltzmann-type distribution, assuming that the long-lived insertion intermediate alcohol ROH* was formed through the insertion reaction of $O(^1D)$ to a C–H bond, along with a low vibrational excitation (less than 0.1 for P_1/P_0). The minor contribution, if any, from such a long-lived complex embedded in the low-N'' regime cannot be ruled out in this work. The vibrationally cold and statistical low-N'' components stand in sharp contrast to our non-statistical low-N'' distribution with high vibrational excitation $P_1/P_0 = 0.75 \pm 0.11$. Such non-statistical dynamics can be considered as a characteristic feature of reactive radical–radical reactions.

5.2.3. $O(^3P) + C_3H_5 \rightarrow C_3H_4O + H$. Figure 9 displays the typical Doppler spectra of the H-atom products obtained using the one-photon resonant $^2P \leftarrow {}^2S$ Lyman-α transition in the VUV region centred at 121.6 nm. The background spectrum (c) was

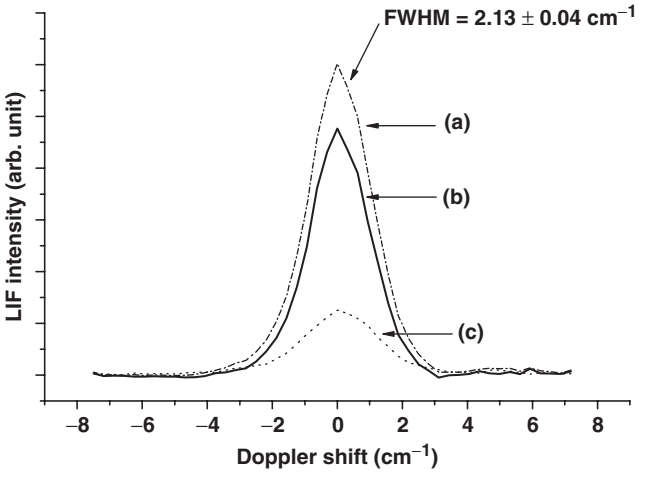

Figure 9. The typical VUV-LIF Doppler spectra of the H-atom products. The interfering background (c) was subtracted from the raw line profile (a) to obtain the pure spectrum (b) due solely to the reaction $O(^3P) + C_3H_5 \rightarrow H(^2S) + C_3H_4O$ under a single collision condition.

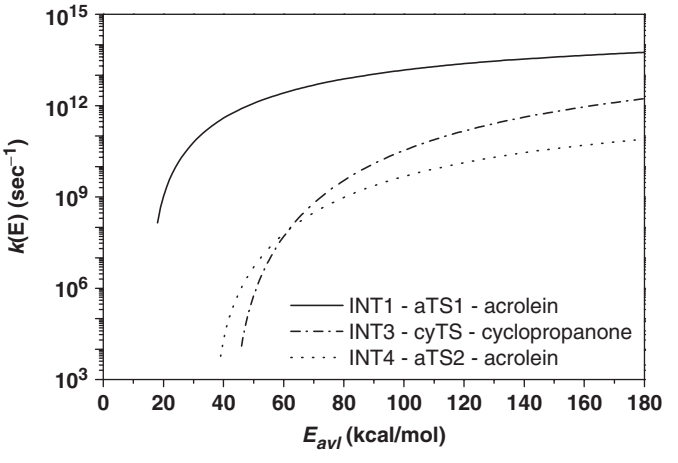

Figure 10. Dependence of the RRKM rate constants on the available energy for the three different single-step channels which lead to the formation of $H(^2S) + C_3H_4O$.

subtracted from the measured raw line profile (a) to obtain the pure spectrum (b). The VUV-LIF spectra of the nascent H atoms show that some fraction of the available energy was released in the form of the translational energy of the $H + C_3H_4O$ products.

The quantitative estimation of the product yields and the relative branching ratios for the competing pathways can be obtained from the energy-specific rate constants k(E). As shown in figure 4(a) and figure 10, the formation of the acrolein + H products from INT1 via aTS1 is calculated to be the most favourable reaction pathway in the available energy range of 0–180 kcal/mol. In particular, under the crossed-beam conditions,

the rate constants through the three competing reaction channels, INT1, INT3, and INT4, are estimated to be 8.4×10^{12}, 1.2×10^{10}, and $5.3 \times 10^{9}\,\mathrm{sec}^{-1}$, respectively. The predominance of the INT1 pathway is mainly ascribed to the activation barrier of aTS1 of the INT1 channel being lower than that of the other two channels which proceed via the transition states cyTS and aTS2 (17.4 versus 45.3 and 38.5 kcal/mol, respectively). The estimated rate constants could be employed as an approximate branching ratio for the competing channels as an initial guideline.

The average fraction of the total available energy partitioned into the translational energy of the $H + C_3H_4O$ products is given by $\langle E_T^{\mathrm{com}} \rangle / E_{avl}$, and was determined to be 0.054 ± 0.002 under our crossed-beam conditions. To better characterize this experimental fraction, the observed translational energy release is compared to the simple prior calculations performed using the Levine–Bernstein method, which predicts that about 0.12 of the available energy is released in the form of translational energy [2, 102].

The discrepancy between the result of the crossed-beam experiment and the prior estimation suggests that the reaction proceeds through the formation of short-lived addition complexes rather than statistical, long-lived intermediates, and that most of the available energy is converted into the internal energy of the polyatomic acrolein product. For the simple unimolecular decomposition of activated HX molecules on a dissociative excited state, a considerable fraction of the available energy is generally transferred to the relative translational energy of the photofragments, and the light H atom carries the bulk of the translational energy due to the disparate mass difference. For the $H + C_3H_4O$ reaction, however, the sufficiently elongated geometry of the loose transition state develops from the highly energized, floppy intermediate, INT1, and the shape of the potential energy surface in figure 4(a) shows a negligible reverse barrier at large internuclear distances as compared to the energy contents of the reaction products. Therefore, the resultant weak, instantaneous repulsive force at the moment of decomposition is not expected to lead to a high fraction of translational energy. The small fraction arising from the loose transition state in this work shows a sharp contrast with those in the previous studies of the reactions of $O(^3P)$ and $C(^3P)$ with neutral, closed-shell hydrocarbon species, where the observed large fraction was ascribed to the existence of the tight transition state along the exit channel [102, 103]. It is not surprising that the non-statistical dynamics in this study is highly sensitive to the detailed shape of the potential energy surface. The loose, product-like transition state with a negligible reverse barrier is believed to lead to the observed low kinetic energy release at the moment of decomposition, which is the unique feature of extremely reactive radical–radical scattering processes.

5.3. *Reaction dynamics of $O(^3P)$ with C_3H_3*

5.3.1. *Ab initio* potential energy surface. The schematic diagram of the reaction pathways in figure 11 illustrates the typical addition and abstraction reactions on the lowest doublet potential energy surface. The barrierless association of $O(^3P)$ with C_3H_3 due to the long-range attractive interaction between reactant radicals, is predicted to lead to several energy-rich addition intermediates. The addition of $O(^3P)$ to the carbon(1) forms a π-conjugated aldehyde intermediate, INT1 ($CHOCCH_2$), while its addition to the carbon(1) and central carbon(2) forms an O-atom bridged oxirane

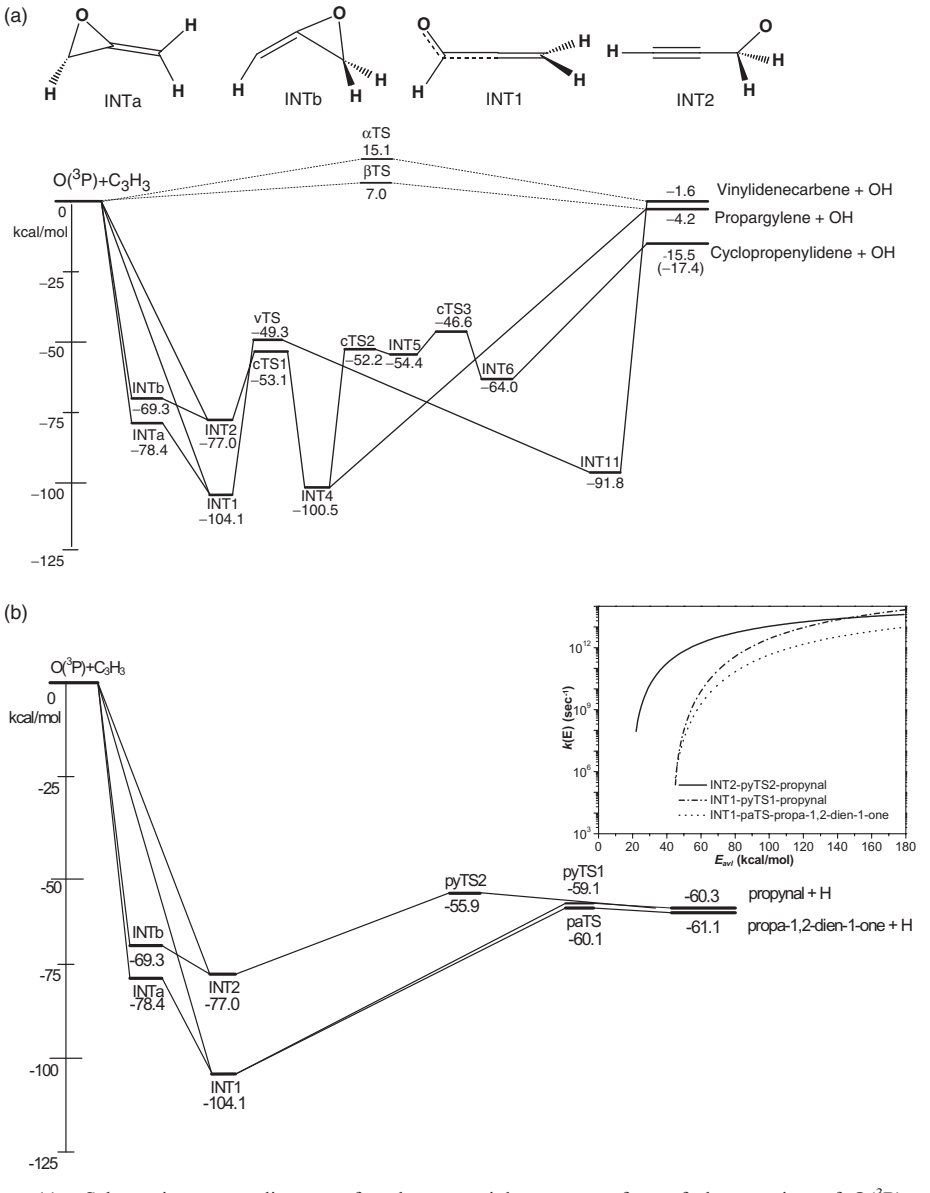

Figure 11. Schematic energy diagrams for the potential energy surface of the reaction of $O(^3P)$ with the propargyl radical at the CBS-QB3 level of the theory. The values in parentheses denote the experimental values (kcal/mol). (a) Pathways to the formation of $OH + C_3H_2$ and (b) pathways to the formation of $H(^2S) + C_3H_2O$. The optimized geometries of the various species are shown in the Supplementary Materials.

intermediate (denoted as INTa). However, INTa is computed to undergo prompt ring-opening conversion to INT1 by the breaking of the C(2)–O bond. On the other hand, the addition of $O(^3P)$ to the carbon(3) produces an intermediate, INT2 ($CHCCH_2O$), which is 27.1 kcal/mol less stable than INT1, whereas its addition to the central

carbon(2) and carbon(3) produces another oxirane intermediate, INTb, lying 9.1 kcal/mol above INTa. INTb also experiences fast ring opening isomerization to form INT2 by the breaking of the C(2)–O bond. Since the two addition intermediates, INT1 and INT2, possess plentiful internal energy, due to their deep potential wells relative to the reactants, neither of the two energy-rich intermediates are expected to redissociate into the reactant radicals, but rather to undergo subsequent isomerization and/or decomposition steps leading to a variety of products [24]. In contrast, the common reaction mechanism observed in the reactions of $O(^3P)$ with saturated hydrocarbons, such as the direct H-atom abstraction pathway through a collinear geometry, is not predicted to occur in our low collision energy regime. For the $O(^3P)$–C_3H_3 system, the centre-of-mass collision energy, E_{com}, is estimated to be at most ca. 6.1 kcal/mol under the full expansion of the radical beams. As clearly shown in figure 11(a), the collision energy is insufficient to overcome the activation barriers along the reaction coordinates for the direct abstraction processes [104, 105].

It is predicted from the *ab initio* calculations that the most facile reaction pathway is the formation of $C_3H_2O + H$, as shown in figure 11(b). C_3H_2O is known to have two different structural isomers, viz. propa-1,2-dien-1-one ($OCCCH_2$) and propynal (CHCCHO), which show nearly the same reaction exothermicities. The reaction channels are in fact simple oxygen–hydrogen exchange reactions, and both of the highly energized intermediates, INT1 and INT2, are calculated to lead to the products. INT1 might undergo either the direct C(1)–H bond rupture through the transition state paTS to yield the products, $OCCCH_2 + H$, or the direct C(3)–H bond rupture through the transition state pyTS1 to yield the products, $CHCCHO + H$. In the case of INT2, the direct cleavage of the C(3)–H bond is expected to yield $CHCCHO + H$ after overcoming the transition state pyTS2 with its relatively low barrier of 21.1 kcal/mol. The major pathway of the three competing single-step channels is believed to be the INT2 channel leading to the formation of propynal + H, because of its low activation barrier, notwithstanding the slightly lower reaction exothermicity. Figure 11 illustrates the RRKM rate constants as a function of E_{avl} for the three competing pathways leading to the formation of $C_3H_2O + H$ under the crossed-beam conditions. In comparison to the other two channels, the unimolecular decomposition rate from INT2 is estimated to be larger, due to the lower activation barrier.

In the reaction $O(^3P) + C_3H_3 \rightarrow C_3H_2 + OH$, the counterpart species of the probed OH product, C_3H_2, is known to be one of three distinctive carbene isomers in the ground electronic state: vinylidenecarbene ($^1CCCH_2$), propargylene (^3HCCCH) and aromatic cyclopropenylidene (^1c-C_3H_2) [106, 107].

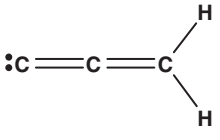

Vinylidenecarbene

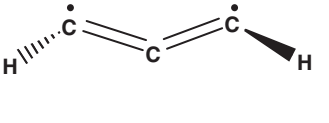

Propargylene

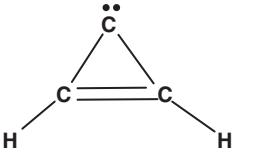

Cyclopropenylidene

In comparison to those carbenes shown above, the corresponding higher energy-state carbene isomers with different spin multiplicities, i.e., $^3CCCH_2$, ^1HCCCH and ^3c-C_3H_2, are calculated to be significantly less stable by 28.9, 12.6, and

70.1 kcal/mol, respectively. Therefore, the resultant endothermic reactions producing such highly unfavourable species are disregarded in our low collision energy regime. In the case of the vinylidenecarbene channel, INT1 is predicted to undergo H-atom migration from carbon(1) to the oxygen atom to form $HOCCCH_2$, followed by direct decomposition to vinylidenecarbene + OH. In the case of the propargylene and aromatic cyclopropenylidene channels, INT2 first involves the H-atom migration from carbon(3) to the oxygen atom to form CHCCHOH. Afterwards, CHCCHOH might undergo either direct bond rupture to form propargylene + OH, or nearly concerted [1,2]-H-atom migration and ring closure followed by direct bond rupture to form cyclopropenylidene + OH.

5.3.2. $O(^3P) + C_3H_3 \rightarrow C_3H_2 + OH$. A typical LIF spectrum of the nascent OH($A\ ^2\Sigma^+ - X\ ^2\Pi$) product is exhibited in figure 12(a). The tiny interfering background OH spectrum in figure 12(b) resulted from the minor HONO impurity present in the NO_2 sample. The second background OH signal was ascribed to the exothermic reaction, $O(^3P) + HBr \rightarrow Br + OH(v'')$, where the small amount of HBr impurity stemmed from the precursor pyrolysis. The OH background was, however, found to exist only in the *vibrationally excited* states ($v'' = 0, 1, 2$ with a ratio of 0 : 9 : 1) in the reactive scattering experiment performed by Zare and coworkers [108]. Here, we focused on the analysis of the rotational state distributions in the *pure* $v'' = 0$ state of the OH product free of the contribution from the HBr impurity.

Figure 13 displays the plots of the relative population for the spin–orbit state, $F_2(^2\Pi_{1/2})$. The bimodal feature composed of low- and high-N″ rotational components is evidently exhibited in the Boltzmann plots. The relative rotational populations

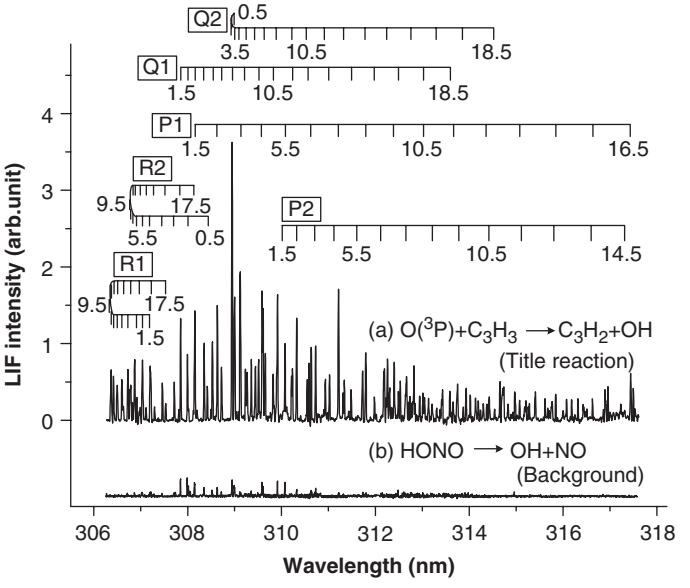

Figure 12. (a) The LIF spectrum in the 0–0 band region of the nascent OH ($A\ ^2\Sigma^+ - X\ ^2\Pi$) produced in the reaction of $O(^3P)$ with the propargyl radical. (b) The background OH produced in the photolysis of the HONO impurity.

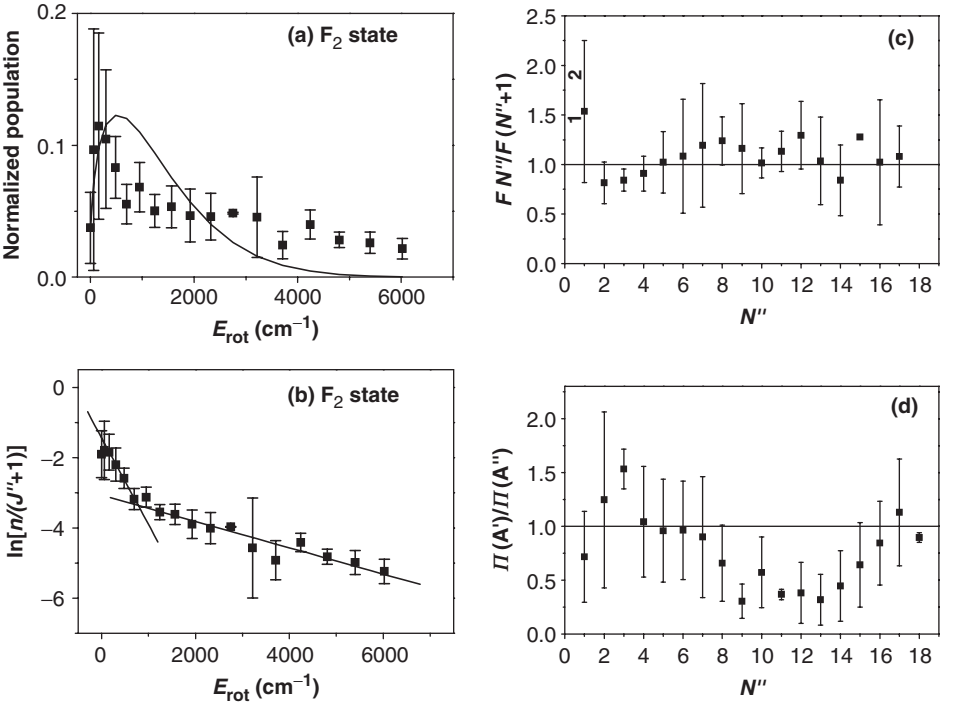

Figure 13. (a) Normalized rotational populations (filled squares) with statistical *prior* (—) plots for the nascent OH produced in the reaction of O(^{3}P) with the propargyl radical for the F_2 state of $v'' = 0$. (b) Boltzmann plots of the nascent OH distributions as a function of the rotational energy for the F_2 state of $v'' = 0$. (c) Spin–orbit state population ratios and (d) Λ-doublet population ratios for $v'' = 0$.

for the two fine spin–orbit electronic states, $F_1(^2\Pi_{3/2})$ and $F_2(^2\Pi_{1/2})$, can be determined. The ratio, 1.09 ± 0.34, refers to the no spin–orbit preference in the $v'' = 0$ state (table 2 and figure 13b). The Λ-doublet propensity in the OH(X $^2\Pi$) radical state distributions was also examined. The averaged ratios of $\Pi(A')/\Pi(A'')$ for $N'' \geq 8$ were determined to be 0.60 ± 0.28, representing some dynamic propensity for $\Pi(A'')$ (table 2).

The most feasible pathway yielding the observed OH product among the three competing pathways in figure 11(a) is believed to be the cyclopropenylidene channel, based upon the following energetics and structural features. First, the rotational energy of up to ca. 6750 cm^{-1} observed in the nascent OH distributions in figure 13 can only be explained in terms of the higher reaction exothermicity of the cyclopropenylidene channel. The maximum available energies, E_{avl}, of the probed OH product for the three different channels are estimated to be 2690, 3600 and 7560 cm^{-1}, respectively. Second, even though the vinylidenecarbene and propargylene channels evidently require fewer steps than the cyclopropenylidene channel, the former two pathways require unfavourable high-energy transition states to be overcome (respective barrier heights of 90.2 and 96.3 vs. 48.5 kcal/mol). Third, in the case of the cyclopropenylidene channel, the cyclic intermediate just prior to dissociation possesses a protruding C–O bond nearly perpendicular to the triangular molecular plane (C–C–O and C–O–H angles: 119.4° and 108.8°). Such a characteristic geometric feature manifests itself in the

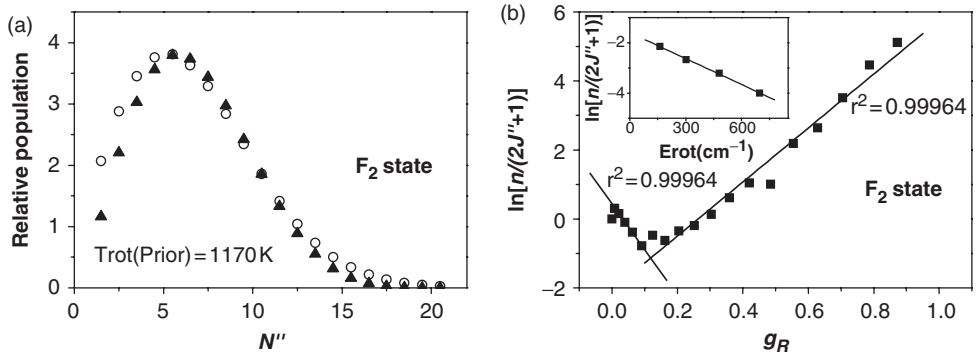

Figure 14. (a) *Prior* (filled triangles) and Boltzmann (open circles) distributions obtained using an average available energy of 21.6 kcal/mol for the F_2 state. (b) A rotational surprisal plot for the nascent OH produced in the reaction of $O(^3P)$ with the propargyl radical for the F_2 state. The inset represents the Boltzmann plot of the deconvoluted populations of the low-N'' components as a function of the rotational energy.

form of a small preferential population of the $\Pi(A'')$ component of OH during the course of the fast bond cleavage. An analogous dynamic propensity has also been observed in the investigation of hydrogen peroxide (H_2O_2) photodissociation, in which the torsional impulse along the HO–OH bond leads to some preference for the $\Pi(A'')$ state [109].

The experimental results were compared to the product state distributions predicted through the aid of the statistical *prior* calculations, in order to better describe the observed bimodal distributions. Figure 14(a) illustrates the prior distributions, together with the estimated rotational temperatures. The prior distributions appeared to be nearly Boltzmann-type over the whole range and predicted considerably lower rotational temperatures (table 2) in comparison to those obtained from the high-N'' regions of the experimental distributions, indicating that some fraction of the nascent OH product exhibits significant rotational excitation. Figure 14(b) shows the rotational surprisals for the low- and high-N'' components. The high-N'' regime is well fitted by the linear surprisal with the large positive slope, indicating that this regime is highly non-statistically populated in comparison to the expected statistical distributions and displays clear dynamic features. Due to the fine surprisal fit, it was possible to deduce the population of the low-N'' regime by subtracting the prior distribution scaled by the surprisal parameter from the nascent distributions. The minor low-N'' regime was found to be adequately characterized by the statistical Boltzmann-type distributions, as depicted in the inset of figure 14(b). Such unusual statistical rotational distributions show that some reactants are likely to proceed through the formation of a long-lived addition complex in the potential energy surface. The relative contributions of the two competing mechanisms could be determined from the ratio of the population partitioning for the low- and high-N'' components, which was estimated to be about 1 : 2.

The observed distinctive bimodal distributions can be rationalized in terms of two competing addition-complex mechanisms: a major short-lived dynamic complex in the high-N'' regime and a minor long-lived statistical complex in the low-N'' regime. There are no other gas-phase studies of the reactions of $O(^3P)$ with hydrocarbon radicals performed in a crossed-beam experiment with which our results

can be compared. The reactions of $O(^3P)$ with saturated hydrocarbons generally proceed via an H-atom abstraction mechanism, resulting in rotationally cold OH products [92, 95, 110, 111]. The reaction pathways also stand in sharp contrast to those observed in the reaction of $O(^3P)$ with allyl in the previous reaction, where the nascent rovibrational distributions displaying totally non-statistical features are governed by a major abstraction process and a minor short-lived addition-complex forming process. Analogous bimodal distributions have been observed to some extent in the case of electronically excited atomic oxygen $O(^1D)$-saturated hydrocarbon reactions [49, 97, 99, 101]. The major high-N'' regime (about 80% of the relative yields) was ascribed to the short-lived insertion process, whereas the minor low-N'' regime was well characterized by the Boltzmann-type long-lived insertion intermediate alcohol formed through the insertion reaction of $O(^1D)$ into a C–H bond. The characteristic reaction mechanisms observed in this work should be considered on the basis of the potential energy surface shown in figure 11. The electronic structures and reactivity of the energy-rich intermediates play an essential role in understanding the microscopic mechanism of gas-phase radical–radical reaction dynamics.

5.3.3. $O(^3P) + C_3H_3 \rightarrow C_3H_2O + H$. The symmetric Doppler-broadened spectra in figure 15 demonstrate that some fraction of the total available energy was partitioned into the translational energy. The average translational energy of the nascent H atoms in the laboratory frame was determined, in order to quantify the amount of energy released. After evaluating 12 individual spectral profiles, the averaged FWHM and $\langle E_T^{lab}(H)\rangle$ values were determined to be $2.42 \pm 0.09\,cm^{-1}$ and 5.15 ± 0.35 kcal/mol, respectively. The averaged $\langle E_T^{lab}(O - C_3H_3)\rangle$ and $\langle E_T^{com}\rangle$ values were 8.58 and 5.09 ± 0.36 kcal/mol, respectively.

To characterize the dynamic features of the reaction pathway, the observed kinetic energy release of the nascent atomic hydrogen was compared with that predicted

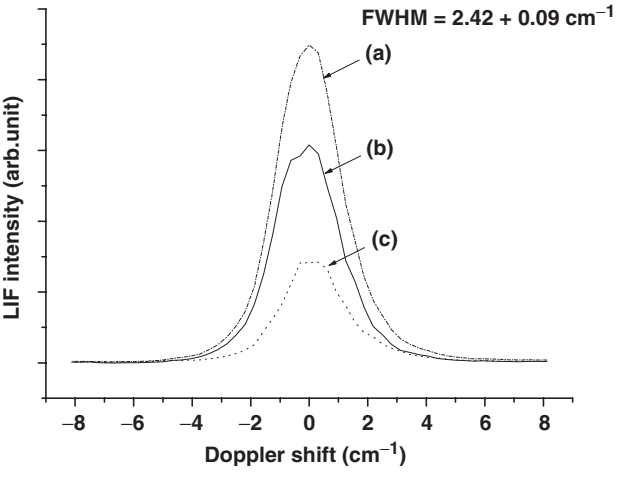

Figure 15. Typical VUV-LIF Doppler spectra of the H-atom products. The interfering background (c) was subtracted from the measured raw line shape (a) to obtain the pure H atom spectrum (b) due solely to the reaction $O(^3P) + C_3H_3 \rightarrow H(^2S) + C_3H_2O$ under single collision conditions.

by statistical prior theory. Under the crossed-beam condition, the average fraction of the total available energy (66.4 kcal/mol) partitioned into the translational energy of the H + propynal products, $\langle E_T^{com} \rangle / E_{avl}$, is estimated to be approximately 7.7%, whereas that predicted by the prior calculation is about 15%.

Such a distinctive discrepancy between the results of the crossed-beam experiment and those of the prior calculation strongly implies that the reaction proceeds through the formation of short-lived, dynamic addition complexes, rather than long-lived, statistical intermediates. Furthermore, most of the available energy is released in the form of the internal excitation of the polyatomic propynal product. The observed small fraction can be rationalized in terms of both the characteristic loose transition state, pyTS2, and the adiabaticity of the excess available energy of INT2. It is clearly shown in figure 11 that the loose geometry of pyTS2 results from the highly floppy INT2, with its large energy content with respect to the radical reactants, and the negligible reverse activation barrier. These unique aspects in the potential energy surface would be expected to result in an ineffective repulsive force being exerted on the sufficiently elongated pyTS2 at the moment of decomposition and on the product fragments along the exit channel. Besides, due to the so-called adiabaticity in disposing of the excess energy left after surmounting the activation barrier, the excess translational and internal energies appear in the form of translational and internal energies in the products, respectively [2]. Therefore, the excess energy of the addition intermediates tends to be manifested in the form of the large internal energy of INT2, which finally appears in the form of the internal excitation of the propynal product.

A similar phenomenon was also observed in the crossed-beam studies of $O(^3P)$ with C_3H_5 yielding the H + acrolein (C_3H_4O) product described in the previous section. The fraction of the kinetic energy release was determined to be only 5.4%. The higher fraction found in the present work might be attributable to the fewer internal degrees of freedom of the polyatomic product, propynal, as compared to those of acrolein (number of atoms: 6 vs. 8). This observation contrasts well with the unimolecular photodissociation from a repulsive excited state and/or the bimolecular reactions with a tight transition state along the exit channel. In such cases, a considerable fraction of the available energy generally appears in the form of the relative kinetic energy of the products, and light species such as atomic hydrogen carry most of the translational energy due to the disparate mass difference. The non-statistical dynamics manifested in this study is indicative of the fate of the highly energized intermediate on the potential energy surface, which has a loose, product-like transition state with a negligible reverse barrier. In addition, the observed low kinetic energy release and the adiabaticity of the excess energy can be considered as one of the characteristic attributes of the H-atom release reactions of $O(^3P)$ with organic hydrocarbon radicals in the gas phase.

5.4. *Reaction dynamics of $O(^3P)$ with t-C_4H_9*

5.4.1. *Ab initio* potential energy surface. The energy profile of the reaction pathways is displayed in figure 16. The diagram suggests two distinctive classes of microscopic reaction mechanisms: *addition* and *abstraction*.

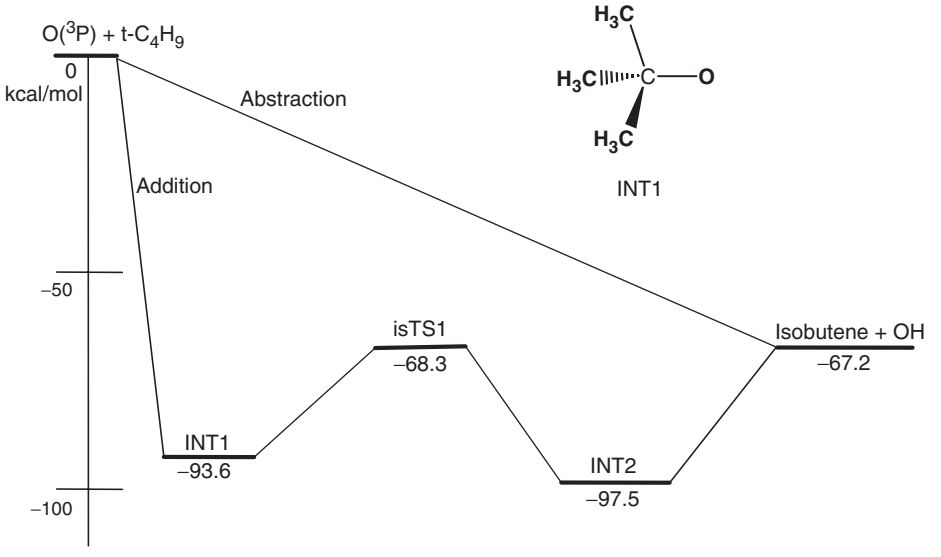

Figure 16. Energy profile of the potential energy surface for the reaction of $O(^3P)$ with t-C_4H_9 at the CBS-QB3 level of theory. The optimized geometries of the various species are shown in the Supplementary Materials.

In the case of the addition process, the diagram shows addition-elimination or addition-isomerization-elimination pathways on the lowest doublet potential energy surface. As the atomic oxygen attacks the t-butyl radical along the entrance reaction coordinate, the long-range attractive interaction between the two reactive reactants causes a barrierless process, which produces an energy-rich addition intermediate denoted as INT1. Since INT1 possesses abundant internal energy, due to its deep potential well, the intermediate can be expected to undergo subsequent isomerization and/or decomposition steps, leading to the formation of a variety of products, rather than redissociation into the reactant radicals. The addition process involves the migration of an H-atom from one of the nine C–H bonds of INT1 to the oxygen atom. This migration leads to the production of $C(CH_3)_2(CH_2)OH$ (denoted as INT2) through the transition state, TS1. Afterwards, INT2 undergoes direct decomposition to yield isobutene + OH products. However, the dominant process is clearly predicted to be the direct H-atom abstraction. In particular, the entrance barrier is estimated to be negligible, in contrast to the substantial barriers reported in the reactions of $O(^3P)$ with closed-shell hydrocarbon molecules, which are in the range of 3–7 kcal/mol [92, 95]. This absence of a substantial barrier can be understood in terms of both the unusually small C−H bond dissociation energy (only 35.5 kcal/mol) of t-C_4H_9 and the highly attractive character of the abstraction process shown in figure 5. In the case of the $O(^3P) + \text{t-}C_4H_9 \rightarrow OH + \text{iso-}C_4H_8$ reaction, due to the transition state corresponding to a very early barrier in the entrance channel and the high exothermicity of the reaction of −67.2 kcal/mol, its extent is expected to be particularly significant, thereby giving rise to a direct, barrierless abstraction channel. The similar absence of a substantial barrier was also described in the previous section in the abstraction pathway of $O(^3P)$ with an allyl radical ($\Delta H = -46.0$ kcal/mol), as shown in figure 5.

5.4.2. $O(^3P) + t\text{-}C_4H_9 \rightarrow iso\text{-}C_4H_8 + OH$. The typical LIF spectra of the nascent OH ($X^2\Pi$: $v'' = 0, 1, 2$) products are displayed in figure 17. These spectra demonstrate considerable rovibrational excitation. The population analyses for the spin–orbit state of $F_1(^2\Pi_{3/2})$ in figure 18 show that the $v'' = 0$ level is described by a bimodal feature composed of low- and high-N'' rotational components, whereas the $v'' = 1$ and 2 levels exhibit unimodal distributions. No noticeable spin–orbit or Λ-doublet preference was observed in any vibrational state (table 2). The averaged vibrational partitioning ratio with respect to the low-N'' components for the $v'' = 0$ level was estimated to be $P_0 : P_1 : P_2 = 1 : 1.17 \pm 0.24 : 1.40 \pm 0.11$, indicating that the nascent vibrational distributions of the OH products are highly excited.

On the basis of the nascent bimodal distributions and *ab initio* calculations, the reaction mechanism at the molecular level can be understood in terms of two competing dynamic pathways: the major direct abstraction process leading to the inversion of the vibrational populations, and the minor short-lived addition-complex process responsible for the hot rotational distributions in the $v'' = 0$ level. The prior estimations predict different rotational temperatures and much lower vibrational partitioning (P_0: P_1: $P_2 = 1$: 0.05: 0.003), as summarized in table 2. Surprisal analysis based upon the prior populations was also performed for the $v'' = 0$ level. Due to the poor surprisal fit, however, it was not possible to deconvolute the rotational populations in order to deduce the relative contribution of each mechanism, except for the large negative slope in the low-N'' region, indicating that the low rotational components are highly populated compared to the statistical prediction. Such a discrepancy clearly demonstrates the dynamic characteristics in the reactive $O(^3P) + t\text{-}C_4H_9$ process, where the fast and random decomposition of the short-lived, energized intermediates leads to the observed non-preferential distributions in the Λ-doublet and spin–orbit states.

The competing reaction pathways contrast well with the oxidation reaction mechanisms of both the saturated hydrocarbon molecules and unsaturated propargyl radical. The former proceeds through the well-known collinear abstraction mechanism, whereas the latter is described only in terms of the addition pathway. Similar reaction mechanisms have been observed in the reaction of $O(^3P)$ with a π-conjugated allyl radical, where both the facile H-atom abstraction and the barrierless addition lead to the formation of stable allene + OH products via competing reaction mechanisms. It has been shown that the distinctive mechanistic features in this study can be understood on the basis of the crossed-beam and *ab initio* investigations. As manifested above, the combined analyses of the nascent rovibrational distributions and the reactivities of the various intermediates involved along the reaction coordinate on the potential energy surface provide a detailed understanding of the extremely reactive radical–radical scattering processes.

6. Summary

A series of studies of the gas-phase reaction dynamics of $O(^3P)$ with hydrocarbon radicals such as allyl (C_3H_5), propargyl (C_3H_3) and t-butyl ($t\text{-}C_4H_9$) in a crossed-beam configuration were presented as prototypal radical–radical oxidation reactions.

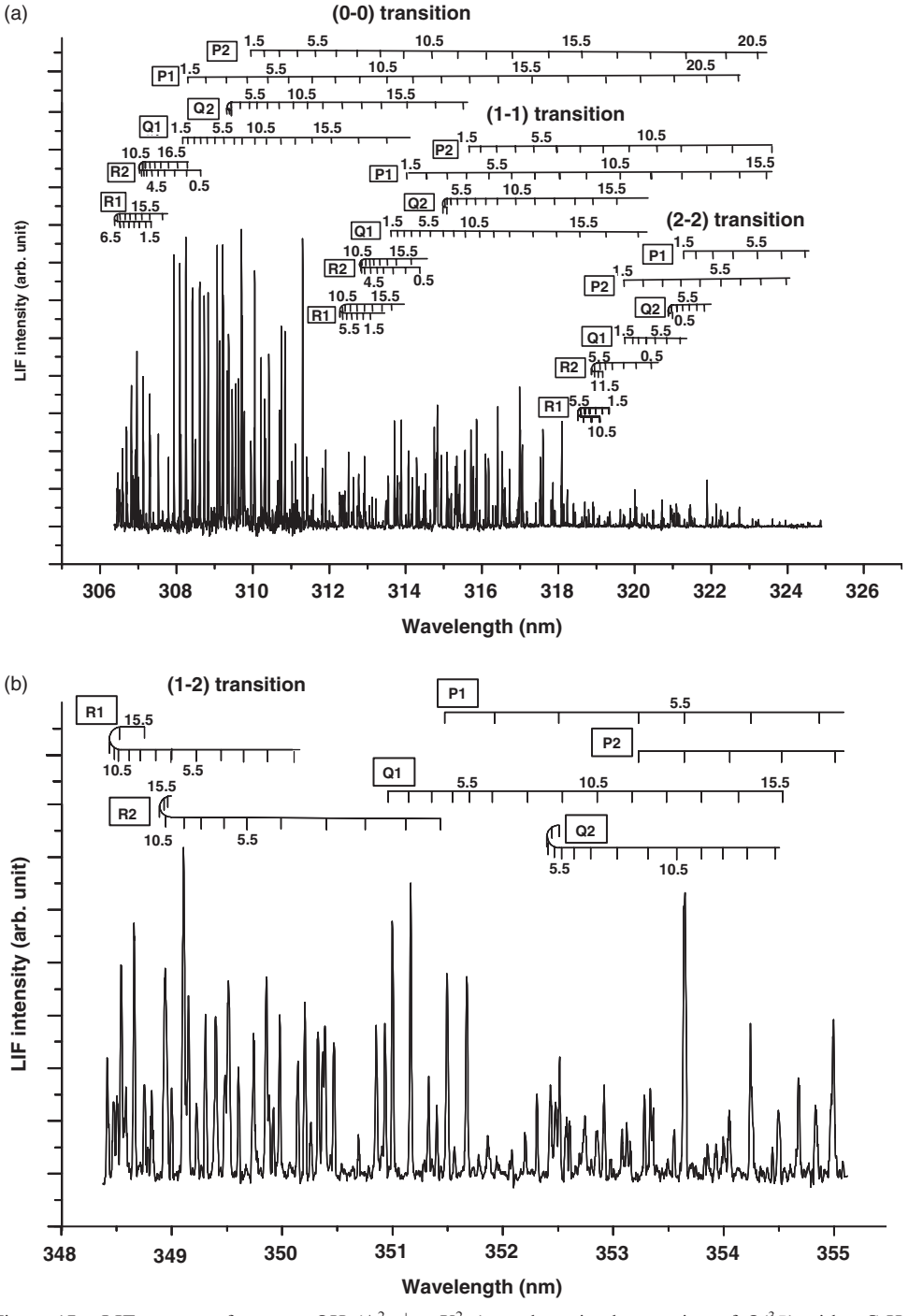

Figure 17. LIF spectra of nascent OH ($A^2\Sigma^+ \leftarrow X^2\Pi$) products in the reaction of $O(^3P)$ with t-C_4H_9. (a) The (0, 0) and (1, 1) diagonal bands and (b) the (1, 2) off-diagonal band.

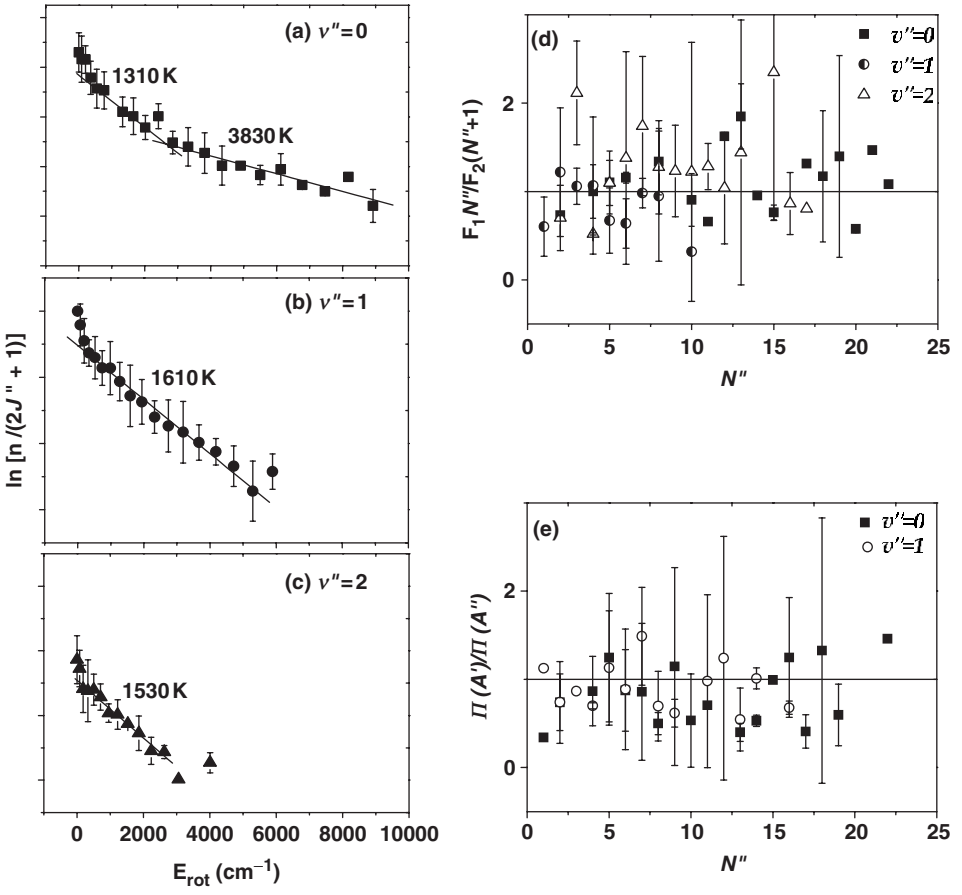

Figure 18. Boltzmann plots of the nascent OH distributions as a function of the rotational energy for the (a) F_1 state of $v''=0$, (b) F_1 state of $v''=1$, and (c) F_1 state of $v''=2$. (d) Spin–orbit state population ratios for $v''=0$ (■), $v''=1$ (Δ), and $v''=2$ (□) in the reaction of $O(^3P)$ with the t-butyl radical. (e) Λ-doublet population ratios for $v''=0$ (■) and $v''=1$ (○) in the reaction of $O(^3P)$ with the t-butyl radical.

With the aid of *ab initio* and statistical calculations, the analyses of the nascent product state distributions probed by high-resolution laser spectroscopy demonstrated the existence of unique competition of abstraction and addition reaction mechanisms and unusual dynamic characteristics. We hope to have provided some valuable insights into the oxidation reactions of various hydrocarbon radicals at the molecular level, which until now have remained unexplored.

Acknowledgments

This work was financially supported by KOSEF-MOST (NRL, R01-2005-000-10582-0) and a Korea Research Foundation Grant (KRF-2004-041-C00166).

References

[1] R. B. Bernstein, *Chemical Dynamics via Molecular Beam and Laser Techniques* (Oxford University Press, New York, 1982).
[2] R. D. Levine and R. B. Bernstein, *Molecular Reaction Dynamics and Chemical Reactivity* (Oxford University Press, New York, 1987).
[3] J. I. Steinfeld, J. S. Francisco, and W. L. Hase, *Chemical Kinetics and Dynamics* (Prentice Hall, New Jersey, 1999).
[4] P. Casavecchia, N. Balucani, and G. G. Volpi, Ann. Rev. Phys. Chem. **50,** 347 (1999).
[5] D. W. Minsek and P. Chen, J. Chem. Phys. **94,** 8399 (1990).
[6] D. W. Kohn, H. Clauberg, and P. Chen, Rev. Sci. Instrum. **63,** 4003 (1992).
[7] D. W. Minsek and J. A. Blush, J.Chem. Phys. **96,** 2025 (1992).
[8] J. Küpper, J. M. Merritt, and R. E. Miller, J. Chem. Phys. **117**, 647 (2002) and references therein.
[9] T. Schultz and I. Fischer, J. Chem. Phys. **107,** 8197 (1997).
[10] T. Schultz and I. Fischer, J. Chem. Phys. **109,** 5812 (1998).
[11] H. J. Deyerl, T. Gilbert, I. Fischer, and P. Chen., J. Chem. Phys. **107,** 3329 (1997).
[12] H. J. Deyerl, I. Fischer, and P. Chen, J. Chem. Phys. **110,** 1450 (1999).
[13] H. J. Deyerl, I. Fischer, and P. Chen, J. Chem. Phys. **111,** 3441 (1999).
[14] I. Fischer, Chimia **54,** 96 (2000).
[15] D. J. Donalson and D.G. Watson, Chem. Phys. **68,** 95 (1982).
[16] D. J. Donalson, I. V. Okuda, and J. J. Sloan, Chem. Phys **193,** 37 (1995).
[17] Z. Min, R. W. Quandt, T.-H. Wong, and R. Bersohn, J. Chem. Phys. **111,** 7369 (1999).
[18] H. K. Kim, H. C. Kwon, J. H. Park, Y. S. Choi, and J. H. Choi, Bull. Korean Chem. Soc. **20,** 1441 (1999).
[19] H. C. Kwon, J. H. Park, H. Lee, H. K. Kim, Y. S. Choi, and J. H. Choi, J. Chem. Phys. **116,** 2675 (2002).
[20] L. K. Kwon, M. J. Nam, S. E. Youn, S. K. Joo, H. Lee, and J.-H. Choi, J. Chem. Phys. **124,** 204320 (2006).
[21] J. H. Park, H. Lee, H. C. Kwon, H. K. Kim, Y. S. Choi, and J. H. Choi, J. Chem. Phys. **117,** 2017 (2002).
[22] H. Lee, S. K. Joo, L. Kwon, and J.-H. Choi, J. Chem. Phys. **119,** 9337 (2003).
[23] H. Lee, S. K. Joo, L. Kwon, and J.-H. Choi, J. Chem. Phys. **120,** 2215 (2004).
[24] H. Lee, M. J. Nam, and J.H. Choi, J. Chem. Phys. **124,** 044311 (2006).
[25] M. J. Nam, S. E. Youn, L. Li, and J. H. Choi, J. Chem. Phys. **123,** 211105 (2006).
[26] S. C. Park, B. J. Braams, and J. M. Bowman, J. Theor. Comput. Chem. **4,** 163 (2005).
[27] B. Wang, H. Hou, and Y. Gu, Chem. Phys. Lett. **304,** 278 (1999).
[28] H. Hou, B. Wang, and Y. Gu, J. Phys. Chem. A **103,** 8075 (1999).
[29] J. H. Park, H. Lee, and J.-H. Choi, J. Chem. Phys. **119,** 8966 (2003).
[30] M. J. Nam, S. E. Youn, and J. H. Choi, J. Chem. Phys. **124,** 104307 (2006).
[31] J. Pacansky and J. S. Chang, J. Chem. Phys. **74,** 5539 (1981).
[32] K. M. Leung and R. P. Lindstedt, Combust. Flame **102,** 129 (1995).
[33] R. D. Kern, H. Chen, J. H. Kiefer, and P. S. Mudipalli, Combust. Flame **100,** 177 (1995).
[34] A. Fahr, P. Hassanzadeh, B. Laszlo, and R. E. Huie, Chem. Phys. **215,** 59 (1997).
[35] L. Yuan, J. DeSain, and R. F. Curl, J. Mol. Spectrosc. **187,** 102 (1998).
[36] D. B. Atkinson and J. W. Hudgens, J. Phys. Chem. A. **103,** 4242 (1999).
[37] X. Krokidis, N. W. Moriarty, W. A. Lester Jr, and M. Frenklach, Chem. Phys. Lett. **314,** 534 (1999).
[38] T. Gilbert, R. Pfab, I. Fischer, and P. Chen, J. Chem. Phys. **112,** 2575 (2000).
[39] J. A. Miller and S. J. Klippenstein, J. Phys. Chem. A. **105,** 7254 (2001).
[40] I. R. Slagle, J. R. Bernhardt, D. Gutman, M. A. Hanning-Lee, and M. J. Pilling, J. Phys. Chem **94,** 3652 (1990).
[41] I. R. Slagle, G. W. Gmurczyk, L. Batt, and D. Gutman, Symp. Int. Combust. Proc. **23,** 115 (1991).
[42] W. R. Gentry and C. F. Giese, Rev. Sci. Instrum. **49,** 595 (1978).
[43] J. Miyawaki, T. Tsuchizawa, K. Yamanouchi, and S. Tsuchiya, Chem. Phys. Lett. **165,** 168 (1990).
[44] D. Stranges, M. Stemmler, X. Yang, J. D. Chesko, A. G. Suits, and Y. T. Lee, J. Chem. Phys. **109**, 5372 (1998) and references therein.
[45] M. Zierhut, W. Roth, and I. Fischer, J. Phys. Chem. **108,** 8125 (2004).
[46] W. H. Smith, J. Chem. Phys. **53,** 792 (1970).
[47] R. A. Sutherland and R. A. Anderson, J. Chem. Phys. **58,** 1226 (1972).
[48] G. M. Jursich and J. R. Wisenfeld, Chem. Phys. Lett. **119,** 511 (1985).
[49] K. Honma, J. Chem. Phys. **99,** 7677 (1993).
[50] H. Okabe, *Photochemistry of Small Molecules* (Wiley-Interscience, New York, 1978).
[51] G. Hilber, A. Lago, and R. Wallenstein, J. Opt. Soc. Am. B **4,** 1753 (1987).
[52] J. P. Marangos, N. Shen, H. Ma, M. H. R. Hutchinson, and J. P. Connerade, J. Opt. Soc. Am. B **7,** 1254 (1990).

[53] K. Tonokura, T. Murasaki, and M. Koshi, Chem. Phys. Lett. **319,** 507 (2000).
[54] C. Lee, W. Yang, and R. G. Parr, Phys. Rev. B **37,** 785 (1988).
[55] T. Ziegler, Chem. Rev. **91,** 65 (1991).
[56] G. A. Petersson and M. A. Al-Laham, J. Chem. Phys. **94,** 6081 (1991).
[57] G. A. Petersson, T. G. Tensfeldt, and J. A. Montgomery Jr, J. Chem. Phys. **94,** 6091 (1991).
[58] A. D. Becke, J. Chem. Phys. **98**, 5648 (1993) and references therein.
[59] J. A. Montgomery Jr, J. W. Ochterski, and G. A. Petersson, J. Chem. Phys. **101,** 5900 (1994).
[60] J. Baker, M. Muir, and J. Andzelm, J. Chem. Phys. **102,** 2063 (1995).
[61] M. W. Wong, Chem. Phys. Lett. **256,** 391 (1996).
[62] J. W. Ochterski, G. A. Petersson, and J. A. Montgomery, J. Chem. Phys. **104,** 2598 (1996).
[63] L. A. Curtiss, K. Raghavachari, P. C. Redfern, and J. A. Pople, J. Chem. Phys. **106,** 1063 (1997).
[64] G. A. Petersson, D. K. Malick, W. G. Wilson, J. W. Ochterski, J. A. Montgomery Jr., and M. J. Firsch, J. Chem. Phys. **109,** 10570 (1998).
[65] J. A. Montgomery Jr, M. J. Frisch, J. W. Ochterski, and G. A. Petersson, J. Chem. Phys. **110,** 2822 (1999).
[66] M. J. Frisch, G. W. Trucks, H. B. Schlegel, *et al*., GAUSSIAN 98, Revision A.7 (Gaussian, Inc, Pittsburgh, Pennsylvania, 1998).
[67] M. J. Frisch, G. W. Trucks, H. B. Schlegel, *et al*., GAUSSIAN 03, Revision C.1 (Gaussian, Inc., Pittsburgh, Pennsylvania, 2003).
[68] G. H. Dieke and H. M. Crosswhite, J. Quant, Spectrosc. Radiat. Transf. **2,** 97 (1962).
[69] W. L. Dimpfl and J. L. Kinsey, J. Quant, Spectrosc. Radiat. Transf. **21,** 233 (1979).
[70] I. L. Chidsey, D. R. Crosley, and J. Quant, Spectrosc. Radiat. Transf **23,** 187 (1980).
[71] J. Luque and D. R. Crosley, *LIFBASE: Database and Simulation Program (v 1.6)*, SRI International Report MP 99-009 (1999).
[72] P. Andresen, G. S. Ondrey, B. Titze, and E. W. Rothe, J. Chem. Phys. **80,** 2548 (1984).
[73] C. B. Cleveland, G. M. Jurisch, M. Trolier, and J. R. Wisenfeld, J. Chem. Phys. **86,** 3253 (1984).
[74] R. G. Macdonald and K. Liu, J. Chem. Phys. **91,** 821 (1989).
[75] J. H. Choi, M. R. Scholefield, D. Kolosov, and H. Reisler, J. Phys. Chem. **101,** 5846 (1997).
[76] S. N. Suchard, *Spectroscopic Data* Vol. I (IFI/Plenum, New York, 1975).
[77] M. J. Bronikowsk and R. N. Zare, Chem. Phys. Lett. **166,** 5 (1990).
[78] W. Demtroder, *Laser Spectroscopy* (Springer-Verlag, Berlin, 1991).
[79] Y. Matsumi, N. Shafer, K. Tonokra, and M. Kawasaki, J. Chem. Phys. **95,** 4972 (1991).
[80] Y. Matsumi, K. Tonokura, and M. Kawasaki, J. Phys. Chem. **96,** 10622 (1992).
[81] R. A. Brownsword, M. Hilenkamp, T. Laurent, R. K. Vatsa, and H. -R. Volpp, Chem. Phys. Lett. **259,** 375 (1996).
[82] E. Zamir and R. D. Levine, Chem. Phys. **52,** 253 (1980).
[83] M. R. Berman and M. C. Lin, J. Phys. Chem. **87,** 3933 (1983).
[84] T. Baer and W. L. Hase, *Unimolecular Reaction Dynamics* (Oxford University Press, New York, 1996).
[85] K. A. Holbrook, M. J. Pilling, and S. H. Robertson, *Unimolecular Reactions* (John Wiley, New York, 1996).
[86] H. W. Rohrs, C. T. Wickham-Jones, G. B. Ellison, D. Berry, and B. M. Argrow, Rev. Sci. Instrum. **66,** 2430 (1995).
[87] H. Zacharias, M. M. T. Loy, P. A. Roland, and A. S. Sudbo, J. Chem. Phys. **81,** 3148 (1984).
[88] D. H. Levy, Ann. Rev. Phys. Chem. **31,** 197 (1980).
[89] P. C. Engelking, Chem. Rev. **91,** 399 (1991).
[90] L. Batt and R. T Milne, Int. J. Chem. Kinet. **9,** 549 (1977).
[91] L. Batt, R. T. Milne, and R. D. McCulloch, Int. J. Chem. Kinet. **9,** 567 (1977).
[92] P. Andresen and A. C. Luntz, J. Chem. Phys. **72,** 5842 (1980).
[93] G. K. Smith and J. E. Butler, J. Chem. Phys. **73,** 2243 (1980).
[94] J. Han, X. Chen, and B. R. Weiner, Chem. Phys. Lett. **332,** 243 (2000).
[95] K. Kleimermanns and A. C. Luntz, J. Chem. Phys. **77,** 3533 (1982).
[96] A. C. Luntz, J. Chem. Phys. **73,** 1143 (1980).
[97] C. R. Park and J. R. Wiesenfeld, J. Chem. Phys. **95,** 8166 (1991).
[98] Y. Rudich, Y. Hurwitz, G. J. Frost, V. Vaider, and R. Naaman, J. Chem. Phys. **99,** 4500 (1993).
[99] S. I. Wada and K. Obi, J. Phys. Chem. A **102,** 3481 (1998).
[100] M. Gonzalez, M. P. Puyuelo, J. Hernando, R. Sayos, P. A. Enriquez, J. Guallar, and I. Banos, J. Phys. Chem. A, **104**, 521 (2000) and references therein.
[101] J. J. Lin, S. Harich, Y. T. Lee, X. J. Yang, J. Chem. Phys. **110**, 10821 (1999).
[102] X. Huang, G. Xing, and R. Bersohn, J. Chem. Phys. **101,** 5818, and references therein (1994).
[103] R. I. Kaiser, W. Sun, A. G. Suits, and Y. T. Lee, J. Chem. Phys. **107,** 8713 (1997).
[104] Q. Zhang, S. Wang, J. Zhou, and Y. Gu, J. Phys. Chem. A, **106**, 115 (2002).
[105] M. Gonzalez, J. Hernado, J. Millan, and R. Sayos, J. Chem. Phys. **110**, 7326 (1999).

[106] J. Takahashi and K. Yamashita, J. Chem. Phys. **104,** 6613 (1996).
[107] A. M. Mebel, W. M. Jackson, A. H. H. Chang, and S. H. Lin, J. Am. Chem. Soc. **120,** 5751 (1998).
[108] K. G. McKendrick, D. J. Rakestraw, R. Zhang, and R. N. Zare, J. Phys. Chem. **92,** 5530 (1988).
[109] K. H. Gericke, S. Klee, and F. J. Comes, J. Chem. Phys. **85,** 4463 (1986).
[110] G. M. Sweeney and K. G. McKendrick, J. Chem. Phys. **106,** 9182 (1997).
[111] G. M. Sweeney, A. Watson, and K. G. McKendrick, J. Chem. Phys. **106,** 9172 (1997).

Supplementary Materials

Complete structures of chemical species

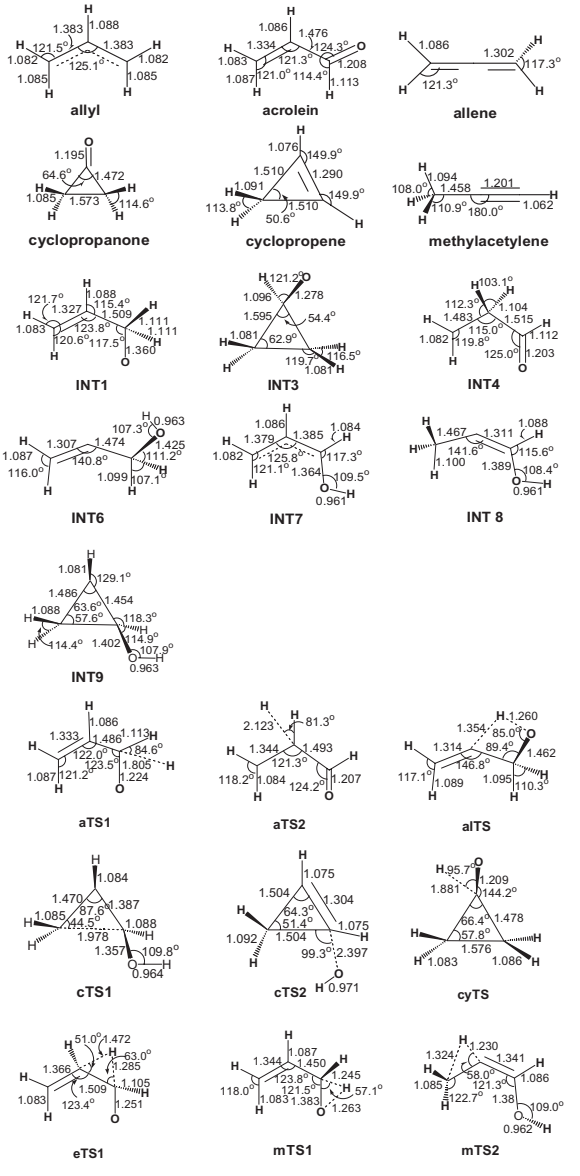

Figure S1.

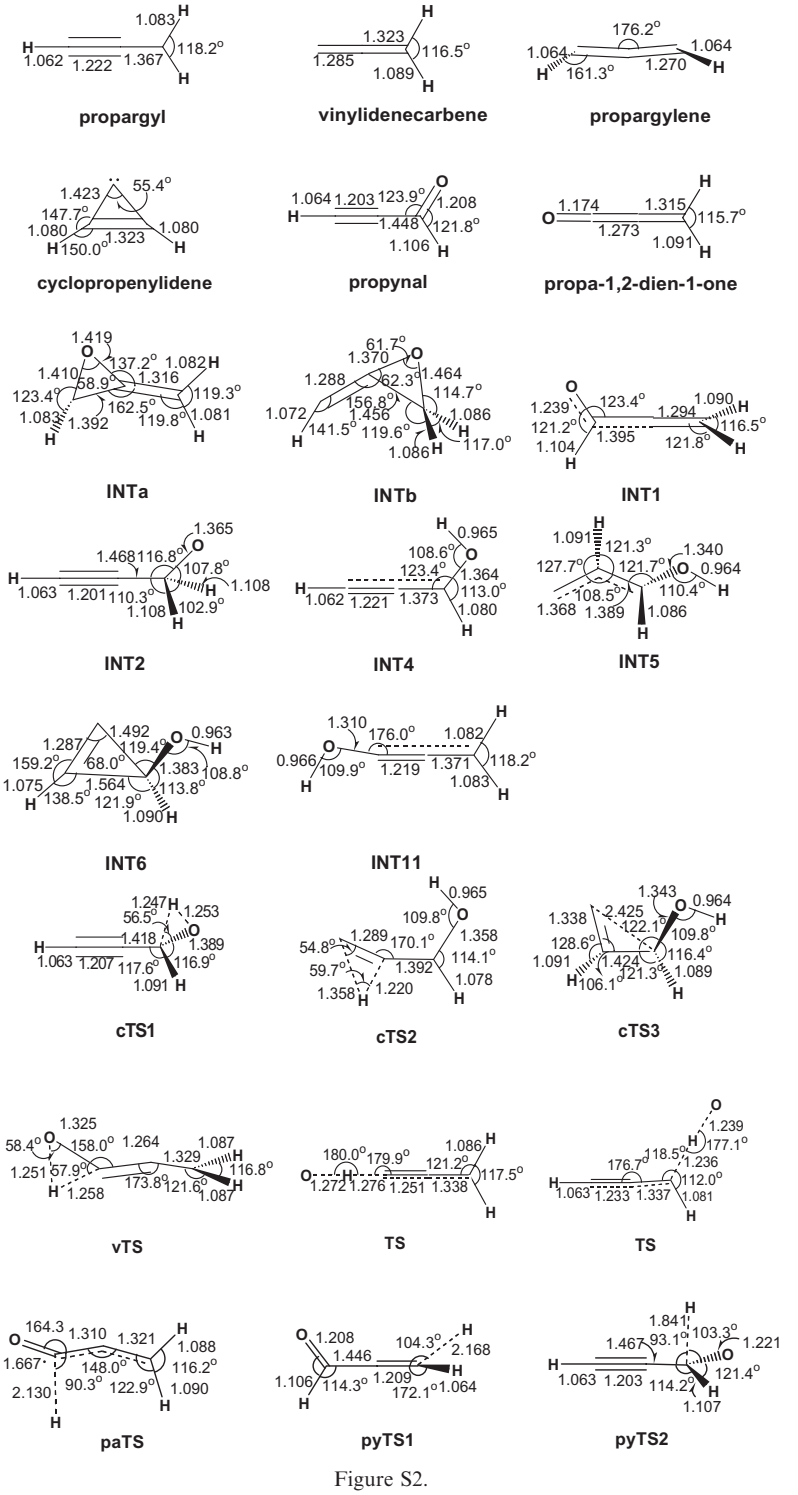

Figure S2.

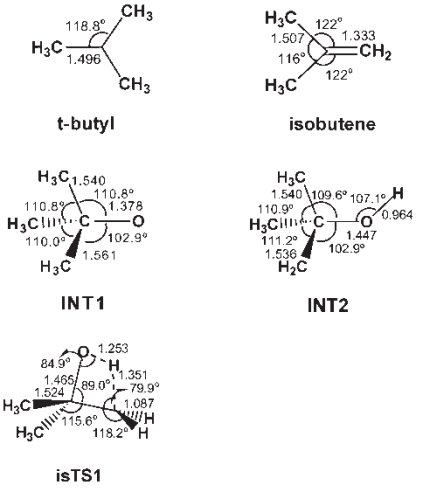

Figure S3.